

Oscillatory Instabilities of a One-Spot Pattern in the Schnakenberg Reaction-Diffusion System in 3-D Domains

Siwen Deng* Justin C. Tzou† Shuangquan Xie‡

Abstract

For an activator-inhibitor reaction-diffusion system in a bounded three-dimensional domain Ω of $\mathcal{O}(1)$ volume and small $\mathcal{O}(\varepsilon^2) \ll \mathcal{O}(1)$ activator diffusivity, we employ a hybrid asymptotic-numerical method to investigate two instabilities of a localized one-spot equilibrium that result from Hopf bifurcations: an amplitude instability leading to growing oscillations in spot amplitude, and a translational instability leading to growing oscillations of the location of the spot's center $\mathbf{x}_0 \in \Omega$. Here, a one-spot equilibrium is one in which the activator concentration is exponentially small everywhere in Ω except in an $\mathcal{O}(\varepsilon)$ localized region about \mathbf{x}_0 where its concentration is $\mathcal{O}(1)$. We find that the translation instability is governed by a 3×3 nonlinear matrix eigenvalue problem. The entries of this matrix involve terms calculated from certain Green's functions, which encode information about the domain's geometry. In this nonlinear matrix eigenvalue system, the most unstable eigenvalue determines the oscillation frequency at onset, while the corresponding eigenvector determines the direction of oscillation. We demonstrate the impact of domain geometry and defects on this instability, providing analytic insights into how they select the preferred direction of oscillation. For the amplitude instability, we illustrate the intricate way in which the Hopf bifurcation threshold τ_H varies with a feed-rate parameter A . In particular, we show that the τ_H versus A relationship possesses two saddle-nodes, with different branches scaling differently with the small parameter ε . All asymptotic results are confirmed by finite elements solutions of the full reaction-diffusion system.

1 Introduction

Research on spot patterns in the three-dimensional (3D) Schnakenberg activator-inhibitor system is driven by applications in fields as diverse as biological morphogenesis (cf. [7], [15]) and chemical reactions (cf. [5], [2]), where understanding the conditions for stability is essential. Localized equilibrium patterns can exhibit a diverse range of complex dynamic behaviors, including spot self-replication, spot annihilation, spot amplitude temporal oscillations, and slow spot drift (cf. [4], [3], [12], [18],[23]).

There has been extensive work in analyzing slow spot drift and spot amplitude temporal oscillations. It is demonstrated in [6, 13, 11] that a single spike in a one-dimensional Gray-Scott model can undergo destabilizing oscillations in either its amplitude or location. **The type of instability that arises first is primarily determined by the feed-rate A , which represents the amount of substrate chemical being pumped into the system.** Typically, amplitude oscillations are triggered at a lower feed-rate than translational oscillatory instabilities. In [22], Hopf bifurcations leading to oscillations in spike heights in the Gierer-Meinhardt model were studied across various ranges of the reaction-time constant. In two dimensions, a comprehensive study of the translational oscillatory instability analysis for the Schnakenberg model is presented in [20] and [25] while the amplitude oscillatory stability is analyzed in [19]. **Moreover, [19] introduced an anomalous scaling of the instability threshold for destabilizing amplitude oscillations, resolving a long-standing open problem in nonlocal eigenvalue problems (NLEP).**

In three-dimensional domains, competition and spot self-replication instabilities of localized spot solutions have been studied for the Schnakenberg [17] and Gierer-Meinhardt models [8]. The former is a global instability that results in the annihilation of one or more spots due to an “over-crowding”, while the latter is a local instability that results in one or more spots self-replicating into two. However, Hopf bifurcations are more intricate in 3D and detailed insights into the translational oscillatory instability and amplitude oscillatory instabilities in 3D remain lacking.

*School of Mathematical and Physical Sciences, Macquarie University, Sydney, Australia; Siwenddeng@gmail.com.

†School of Mathematical and Physical Sciences, Macquarie University, Sydney Australia; tzou.justin@gmail.com.

‡School of Mathematics, Hunan University, Changsha City, Hunan, China; xieshuangquan2013@gmail.com.

Recently, investigations into heterogeneous domains have generated considerable interest. Two types of heterogeneity are introduced in [24]. The first type is a perturbation of a spatially uniform feed rate, and the second involves the inclusion of a defect in the domain. The former type has been considered in some works [9], [10], while the latter has received less attention. The purpose of introducing the second type of heterogeneity is to create an asymmetric pattern, which provides a more general and practical research scenario relevant to real-world applications.

In dimensionless form, the Schnakenberg RD model (cf. [16]) is

$$\begin{aligned} \mathcal{V}_t &= \varepsilon^2 \Delta \mathcal{V} - \mathcal{V} + b + \mathcal{U}\mathcal{V}^2, & x \in \Omega; & \quad \partial_n \mathcal{V} = 0, x \in \partial\Omega, \\ \tau \mathcal{U}_t &= \mathcal{D} \Delta \mathcal{U} + A - \mathcal{U}\mathcal{V}^2, & x \in \Omega; & \quad \partial_n \mathcal{U} = 0, x \in \partial\Omega. \end{aligned} \quad (1.1)$$

Here, \mathcal{V} and \mathcal{U} denote the activator and inhibitor fields, respectively. The domain $\Omega \subset \mathbb{R}^3$ is bounded, while b and A are constant bulk activator and inhibitor feed rates. Additionally, $\mathcal{D} > 0$ and $0 < \varepsilon \ll 1$. To ensure that the amplitude of a local spot in model (1.1) remains $\mathcal{O}(1)$ as $\varepsilon \rightarrow 0$, we introduce the rescaling $\mathcal{V} = \varepsilon^{-3}bv$, $\mathcal{U} = \varepsilon^3b^{-1}u$, $\tau = \varepsilon^3b^{-2}\tau$, $\mathcal{D} = \varepsilon^{-4}b^{-2}D$, and $A = b^{-1}A$. We then obtain the rescaled, singularly perturbed Schnakenberg model.

$$\begin{aligned} v_t &= \varepsilon^2 \Delta v - v + \varepsilon^3 + uv^2, & x \in \Omega; & \quad \partial_n v = 0, x \in \partial\Omega, \\ \tau u_t &= \frac{D}{\varepsilon} \Delta u + A - \varepsilon^{-3}uv^2, & x \in \Omega; & \quad \partial_n u = 0, x \in \partial\Omega. \end{aligned} \quad (1.2)$$

In (1.2), the Hopf bifurcation parameter τ measures the rate at which the inhibitor responds to perturbations in the concentrations of the activator and inhibitor. As τ increases, the inhibitor's response becomes progressively slower, leading to oscillatory instabilities via Hopf bifurcations.

In this paper, we consider the effect of increasing the parameter τ on a single spot in a bounded 3D domain Ω , which may be either a localized heterogeneous domain or a normal domain. Two types of oscillatory instabilities are presented. First, motivated by [20], we perform a stability analysis of the spot's motion (position). In particular, we analyze the effect of geometric asymmetry on the instability threshold and the preferred direction of the spot's oscillation. The associated linearized eigenvalue problem has an eigenfunction of the form $\Psi(r)Y_n^m(\varphi, \theta)$, where Y_n^m is the Spherical Harmonics. The translation mode is $n = \pm 1$ for which the corresponding eigenvalue is small as $\varepsilon \rightarrow 0$. We therefore refer this problem as *small* eigenvalue problem. Second, we provide a detailed study of temporal oscillations in the spot amplitude, referred as *large* eigenvalue problem, corresponding to the mode $n = 0$. One of our key findings is the existence of two regimes: the $\tau \sim \mathcal{O}(1)$ regime and $\tau \sim \mathcal{O}(\varepsilon^{-3})$ regime. Furthermore, there is an overlap between these two regimes for a certain range of A . We investigate the behavior of the Hopf bifurcation threshold τ_H within this interval and present how the stability status of the system changes as τ varies.

The outline of the paper is as follows. In §2, we construct a one-spot equilibrium solution of the Schnakenberg PDE (1.2) basing on the work from [17]. We use the correction terms in $\mathcal{O}(\varepsilon^3)$ in the stability analysis.

In §3, we analyze the translational oscillatory instability of the one spot equilibrium. We perturb $\tau = \varepsilon^{-3}(\tau_0 + \varepsilon\tau_1)$ and $\lambda = \varepsilon^2(\lambda_0 + \varepsilon\lambda_1)$. By applying the solvability conditions on the $\mathcal{O}(\varepsilon^2)$ of the small eigenvalue problem in the inner region, we obtain the leading order of the Hopf bifurcation threshold τ_0 . To compute τ_1 and λ_0 , the solvability conditions are applied again on the $\mathcal{O}(\varepsilon^2)$ of the small eigenvalue problem in the inner region, deriving a 3×3 complex matrix-eigenvalue problem of the form $M\mathbf{a} = \lambda\mathbf{a}$. By setting λ as purely imaginary, we obtain the targeted $\mathcal{O}(\varepsilon)$ correction term for the translational oscillatory instability threshold, the leading order of the corresponding oscillation frequency at onset, and the oscillation direction, which is indicated by the eigenvector \mathbf{a} . The matrix M contains the information of domain geometry, which involves the quadratic terms of the local behavior of Helmholtz Green's function $G_\mu(\mathbf{x}; \mathbf{x}_j)$ satisfying

$$\begin{aligned} \Delta G_\mu - \mu^2 G_\mu &= \delta(\mathbf{x} - \mathbf{x}_j), & \mathbf{x}, \mathbf{x}_j \in \Omega, & \quad \partial_n G_\mu = 0, \quad \mathbf{x} \in \partial\Omega, \\ G_\mu(\mathbf{x}; \mathbf{x}_j) &\sim -\frac{1}{4\pi|\mathbf{x} - \mathbf{x}_j|} + R_\mu(\mathbf{x}_j; \mathbf{x}_j) + (\mathbf{x} - \mathbf{x}_j) \cdot \nabla_{\mathbf{x}} R_\mu(\mathbf{x}; \mathbf{x}_j)|_{\mathbf{x}=\mathbf{x}_j} \\ &\quad + \frac{1}{2}(\mathbf{x} - \mathbf{x}_j)^T \mathcal{H}_{\mu jj}(\mathbf{x} - \mathbf{x}_j) - \frac{\mu^2}{8\pi}|\mathbf{x} - \mathbf{x}_j|, & \text{as } \mathbf{x} \rightarrow \mathbf{x}_j, \\ G_\mu(\mathbf{x}; \mathbf{x}_i) &\sim G_\mu(\mathbf{x}_j; \mathbf{x}_i) + (\mathbf{x} - \mathbf{x}_j) \cdot \nabla_{\mathbf{x}} G_\mu(\mathbf{x}; \mathbf{x}_i)|_{\mathbf{x}=\mathbf{x}_j} + \frac{1}{2}(\mathbf{x} - \mathbf{x}_j)^T \mathcal{H}_{\mu ji}(\mathbf{x} - \mathbf{x}_j), \\ &\quad \text{as } \mathbf{x} \rightarrow \mathbf{x}_i \neq \mathbf{x}_j, \end{aligned} \quad (1.3)$$

where \mathbf{x}_j is the source center, and $\mathcal{H}_{\mu jj}$ and $\mathcal{H}_{\mu ji}$ are the 3×3 Hessian matrices. In §3.1, we apply our result on a unit sphere and compute τ up to $\mathcal{O}(\varepsilon^2)$ correction and λ to $\mathcal{O}(\varepsilon)$ correction, which provides a high accuracy in the numerical experiment. In §3.2, we examine how the geometry select the dominant mode of oscillation. The result shows that the preferred direction of oscillation is along the major axis for which τ is the smallest among all three directions. In §3.3, we further break the domain symmetry by removing a ball-shaped defect from which the chemicals leak out. Following the technique from [24], the defect can be treated as a localized pinned spot and an extra term is introduced into the matrix M in this geometry. Consequently, the dominant mode of oscillation differs from that in the spherical case. The equilibrium solution for the one-spot pattern on a defected domain is provided in Appendix A.

In §4, we analyze the stability of one spot equilibrium with respect to the amplitude oscillatory instability. Specifically, we study the behavior of τ_H when the feed rate A changes. Two regimes of τ_H are discussed. In §4.1, τ_H is $\mathcal{O}(1)$ and a hybrid asymptotic-numerical method is used to determine the threshold. We find a unique threshold when $A < 13.56$, where the system becomes unstable to amplitude oscillatory instability when τ exceeds the threshold and remains stable when it is below the threshold. For $13.56 \leq A < A_\varepsilon$, where A_ε is a saddle point weakly depending on ε , two distinct HB thresholds exist. No bifurcation occurs for $A > A_\varepsilon$ in the $\tau \sim \mathcal{O}(1)$ regime. In §4.2, we study the $\mathcal{O}(\varepsilon^{-3})$ regime, where the values of τ_H depend on the spectrum of the leading order of the eigenvalue problem in the inner region. In this regime, there is a unique threshold for each value of $A > 13.56$. For small τ_0 where $\tau_0 = \varepsilon^3 \tau$, a reduced problem is introduced to investigate the values of τ_H near $A = 13.56$. There is an overlap between these two regimes for a small interval of A . In other words, three HB thresholds appear when $13.56 \leq A < A_\varepsilon$: two at $\mathcal{O}(1)$ and one at $\mathcal{O}(\varepsilon^{-3})$. In Figure 1a, a full theoretical result for the large eigenvalue

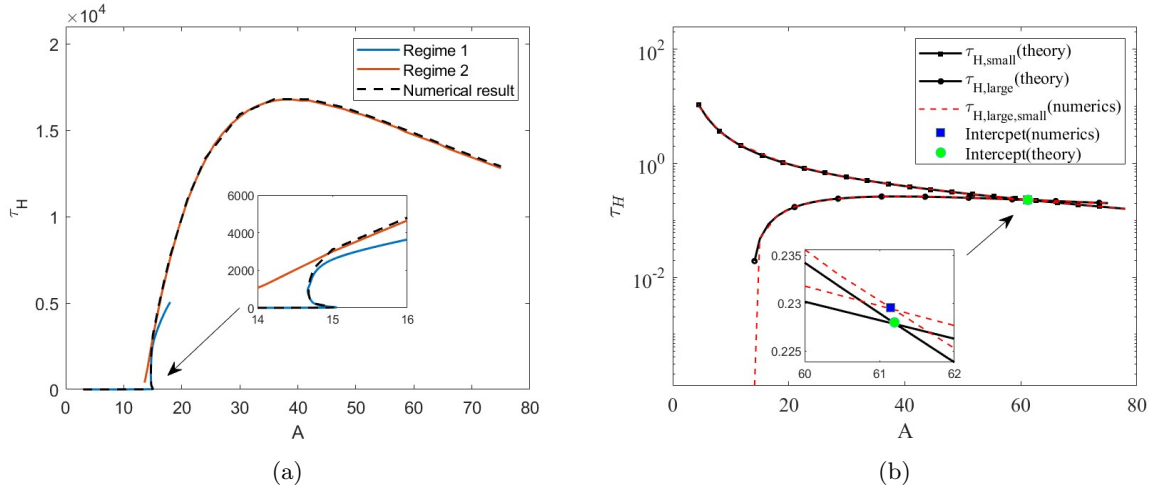


Figure 1: (a) Theoretical value of τ_H in the large eigenvalue problem as a function of A . Two different regimes are found: $\tau_H \sim \mathcal{O}(1)$ regime and $\tau_H \sim \mathcal{O}(\varepsilon^{-3})$ regime. The zoom-in box shows that there are 3 distinct HB thresholds when $13.56 < A < 13.98$. (b) We plot the HB values for amplitude and position oscillations for $\varepsilon = 0.03$. The numerical results coincide with our theoretical results in both figures.

problem is present. The line of regime 1 is the $\mathcal{O}(1)$ HB threshold while the line of regime 2 refers to $\mathcal{O}(\varepsilon^{-3})$ threshold. As shown in the zoom-in box, When A is approaching to 13.56 from the right, the value of τ_H tends to infinity, and there are 3 distinct thresholds when $13.56 \leq A < 13.98$ as we claimed. In Figure 1b, we plot the Hopf bifurcation threshold for both large eigenvalue problems and small eigenvalue problems. The figure shows that they intercept at $A = 61.2$.

A full numerical solution of (1.2) is performed in §5 to confirm our theoretical results. Finally, in §6, we conclude with a briefly discussion.

2 Equilibrium

In this section, we briefly review the construction process of the equilibrium solution, as completed in [17]. We start by obtaining the one-spot equilibrium solution of (1.2) using the method of matched asymptotic expansions.

In the inner region near the spot, we set $\mathbf{x} = \mathbf{x}(\sigma)$ where $\sigma = \varepsilon^3 t$ represents the slow time scale, and introduce the inner variables

$$\mathbf{x} = \varepsilon \mathbf{y}, \quad \mathbf{y} = \begin{pmatrix} y_1 \\ y_2 \\ y_3 \end{pmatrix} = \rho \mathbf{e}, \quad \mathbf{e} = \begin{pmatrix} \sin \theta \cos \varphi \\ \sin \theta \sin \varphi \\ \cos \theta \end{pmatrix}, \quad (2.1)$$

$$v_e \sim \sqrt{D}(V_\varepsilon(\rho) + \varepsilon^3 V_3(\mathbf{y}) + \dots), \quad u_e \sim \frac{1}{\sqrt{D}}(U_\varepsilon(\rho) + \varepsilon^3 U_3(\mathbf{y}) + \dots),$$

where U_ε and V_ε satisfy the radially symmetric core problem

$$\begin{aligned} \Delta_\rho V_\varepsilon - V_\varepsilon + U_\varepsilon V_\varepsilon^2 &= 0, & V_\varepsilon'(0) &= 0, & V_\varepsilon &\rightarrow 0, & \text{as } \rho &\rightarrow \infty, \\ \Delta_\rho U_\varepsilon - U_\varepsilon V_\varepsilon^2 &= 0, & U_\varepsilon'(0) &= 0 \end{aligned} \quad (2.2)$$

with far-field behavior

$$U_\varepsilon \sim \chi(S_\varepsilon) - S_\varepsilon/\rho + \dots, \quad \text{as } \rho \rightarrow \infty, \quad (2.3)$$

and noted that $\Delta_\rho \equiv \partial_{\rho\rho} + 2\rho^{-1}\partial_\rho$. The $\mathcal{O}(\varepsilon^2)$ terms in the expansion of u_e and v_e are absent under the assumption that the spot is stationary over time. Numerical solutions of (2.2) are presented in [17]. In Figure 2, the nonlinear function $\chi(S_\varepsilon)$ is generated for varies values of S_ε . To avoid the local (mode-2) self-replication instability of the spot,

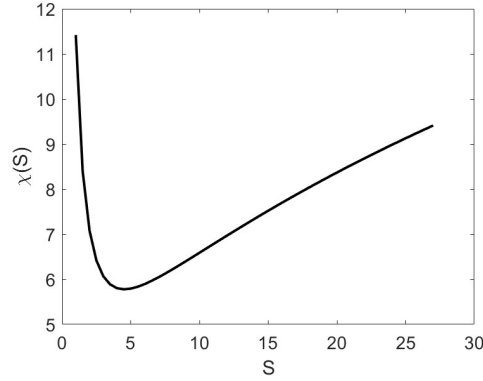


Figure 2: A plot of $\chi(S_\varepsilon)$ versus S_ε . The fold point at $(S_\varepsilon, \chi) \approx (4.52, 5.78)$, where $\chi'(4.52) = 0$.

we impose $S_\varepsilon < \Sigma_2 \approx 20.16$. Applying the divergence theorem on the second equation of (2.2), we obtain

$$S_\varepsilon = \int_0^\infty U_\varepsilon V_\varepsilon^2 \rho^2 d\rho. \quad (2.4)$$

In the outer region, we express the term $\varepsilon^{-3}uv^2$ in (1.2) in the sense of distributions as

$$\varepsilon^{-3}uv^2 \rightarrow 4\pi\sqrt{D} \left(\int_0^\infty U_\varepsilon V_\varepsilon^2 \rho^2 d\rho \right) \delta(\mathbf{x}) = 4\pi\sqrt{D}S_\varepsilon \delta(\mathbf{x} - \mathbf{x}_1), \quad (2.5)$$

where \mathbf{x}_1 is the source location. Therefore, the quasi-equilibrium solution for u in the outer region satisfies

$$\frac{D}{\varepsilon} \Delta u_e + A = 4\pi\sqrt{D}S_\varepsilon \delta(\mathbf{x} - \mathbf{x}_1), \quad \mathbf{x} \in \Omega; \quad \partial_n u_e = 0, \quad \mathbf{x} \in \partial\Omega. \quad (2.6)$$

We directly solve (2.6) to obtain the solution for u in the outer region, namely

$$u_e = \bar{\mu} - \frac{4\pi\varepsilon}{\sqrt{D}} S_\varepsilon G(\mathbf{x}; \mathbf{x}_1), \quad (2.7)$$

where $G(\mathbf{x}; \mathbf{x}_j)$ the Nuemann Green's function satisfying

$$\begin{aligned}\Delta G &= \frac{1}{|\Omega|} - \delta(\mathbf{x} - \mathbf{x}_j), \quad \mathbf{x} \in \Omega; \quad \partial_n G = 0, \quad \mathbf{x} \in \partial\Omega, \\ G(\mathbf{x}; \mathbf{x}_j) &\sim \frac{1}{4\pi|\mathbf{x} - \mathbf{x}_j|} + R_{jj} + \nabla_{\mathbf{x}} R(\mathbf{x}; \mathbf{x}_j)|_{\mathbf{x}=\mathbf{x}_j} \cdot (\mathbf{x} - \mathbf{x}_j) \\ &\quad + \frac{1}{2}(\mathbf{x} - \mathbf{x}_j)^T \mathcal{H}_{jj}(\mathbf{x} - \mathbf{x}_j), \quad \text{as } \mathbf{x} \rightarrow \mathbf{x}_j; \\ G(\mathbf{x}; \mathbf{x}_i) &\sim G_{ij} + \nabla_{\mathbf{x}} G(\mathbf{x}; \mathbf{x}_j)|_{\mathbf{x}=\mathbf{x}_i} \cdot (\mathbf{x} - \mathbf{x}_i) \\ &\quad + \frac{1}{2}(\mathbf{x} - \mathbf{x}_i)^T \mathcal{H}_{ij}(\mathbf{x} - \mathbf{x}_i), \quad \text{as } \mathbf{x} \rightarrow \mathbf{x}_i \neq \mathbf{x}_j,\end{aligned}\tag{2.8}$$

Integrating (2.6) over Ω and applying the divergence theorem yields the solvability condition

$$S_\varepsilon = \frac{A|\Omega|}{4\pi\sqrt{D}},\tag{2.9}$$

where $|\Omega|$ denotes the volume of the domain Ω .

We then match the far-field behavior of the spot in the inner region (2.3) to the leading order term of the outer solution (2.7) using the local behavior of $G(\mathbf{x}; \mathbf{x}_1)$ given in (2.8), yielding an equation

$$\bar{\mu} = 4\pi\varepsilon R_{11} S_\varepsilon + \chi(S_\varepsilon),\tag{2.10}$$

where $R_{11} = R(\mathbf{x}_1; \mathbf{x}_1)$ is the regular part of $G(\mathbf{x}; \mathbf{x}_1)$ when $\mathbf{x} \rightarrow \mathbf{x}_1$.

We emphasize that the Green's function is of $\mathcal{O}(\varepsilon)$ in the outer solution, indicating the absence of $\mathcal{O}(\varepsilon^2)$ terms in the inner region due to the slow spot dynamics described in [17],

$$S_\varepsilon \nabla_{\mathbf{x}} R(\mathbf{x}; \mathbf{x}_1)|_{\mathbf{x}=\mathbf{x}_1} = \mathbf{0}.\tag{2.11}$$

By solving (2.9), (2.10) and (2.11) simultaneously, we obtain the source strength of the spot S_ε , the equilibrium position of the spot, and all other constants.

Expanding the outer solution (2.7) and collecting the $\mathcal{O}(\varepsilon^3)$ terms the system of V_3 and U_3 is obtained, which is

$$\begin{aligned}\Delta V_3 - V_3 + \frac{1}{\sqrt{D}} + U_3 V_\varepsilon^2 + 2U_\varepsilon V_\varepsilon V_3 &= 0, \quad V_3'(0) = 0, \\ \Delta U_3 + \frac{A}{\sqrt{D}} - U_3 V_\varepsilon^2 - 2U_\varepsilon V_\varepsilon V_3 &= 0, \quad U_3'(0) = 0, \\ V_3 \rightarrow \frac{1}{\sqrt{D}}, \quad U_3 \sim -2\pi S_\varepsilon \mathbf{y}^T \mathcal{H}_{11} \mathbf{y}, &\quad \text{as } \mathbf{y} \rightarrow \infty,\end{aligned}\tag{2.12}$$

where \mathcal{H}_{11} is the Hessian matrix of the regular part of $G(\mathbf{x}; \mathbf{x}_1)$ as \mathbf{x} is approaching to the source location. With the inner coordinates ρ and \mathbf{e} defined in (2.1), the far-field condition can be written as

$$U_3 = -2\pi S_\varepsilon \rho^2 \mathbf{e}^T \mathcal{H}_{11} \mathbf{e}, \quad \text{as } \rho \rightarrow \infty.\tag{2.13}$$

This completes the construction of one spot equilibrium solution.

3 The stability analysis: Small eigenvalues

We now analyze the instability of the small eigenvalue problem for a one-spot pattern. Let $|\psi|, |\phi| \ll \mathcal{O}(1)$, we perturbed the equilibrium solution

$$v = v_e(r) + e^{\lambda t} \phi(x), \quad u = u_e(r) + e^{\lambda t} \psi(x),\tag{3.1}$$

which results a eigenvalue problem,

$$\begin{aligned}\varepsilon^2 \Delta \phi - \phi + 2u_e v_e \phi + v_e^2 \psi &= \lambda \phi, \quad \frac{D}{\varepsilon} \Delta \psi - \varepsilon^{-3} (2u_e v_e \Phi + v_e^2 \psi) = \tau \lambda \psi, \quad x \in \Omega; \\ \partial_n \phi &= \partial_n \psi = 0 \quad \text{on } \partial\Omega.\end{aligned}\tag{3.2}$$

In the inner region, we expand ϕ and ψ in the power of ε , namely

$$\begin{aligned}\Phi &\sim \sqrt{D}(\Phi_\varepsilon(\rho) + \varepsilon^2\Phi_2(\mathbf{y}) + \varepsilon^3\Phi_3(\mathbf{y}) + \dots), \\ \Psi &\sim \frac{1}{\sqrt{D}}(\Psi_\varepsilon(\rho) + \varepsilon^2\Psi_2(\mathbf{y}) + \varepsilon^3\Psi_3(\mathbf{y}) + \dots),\end{aligned}\tag{3.3}$$

where $\rho = |\mathbf{y}| = \varepsilon^{-1}|\mathbf{x}| = \varepsilon^{-1}r$, and \mathbf{y} is defined in the equation (2.1).

Substituting (3.3) into (3.2), we derive the leading order system

$$\Delta_{\mathbf{y}} \begin{pmatrix} \Phi_\varepsilon \\ \Psi_\varepsilon \end{pmatrix} + \mathcal{M} \begin{pmatrix} \Phi_\varepsilon \\ \Psi_\varepsilon \end{pmatrix} = \mathbf{0},\tag{3.4}$$

where

$$\mathcal{M} = \begin{pmatrix} -1 + 2U_\varepsilon V_\varepsilon & V_\varepsilon^2 \\ -2U_\varepsilon V_\varepsilon & -V_\varepsilon^2 \end{pmatrix}.\tag{3.5}$$

It is readily observed that the solution to the first equation in (3.4) is a linear combination of $\partial_{y_1} V_\varepsilon$, $\partial_{y_2} V_\varepsilon$, and $\partial_{y_3} V_\varepsilon$. Therefore the solution to (3.4) is given by

$$\Phi_\varepsilon = \mathbf{a} \cdot \nabla_{\mathbf{y}} V_\varepsilon = (\mathbf{a}^T \mathbf{e}) \partial_\rho V_\varepsilon, \quad \Psi_\varepsilon = \mathbf{a} \cdot \nabla_{\mathbf{y}} U_\varepsilon = (\mathbf{a}^T \mathbf{e}) \partial_\rho U_\varepsilon; \quad \mathbf{a} = \begin{pmatrix} a_1 \\ a_2 \\ a_3 \end{pmatrix},\tag{3.6}$$

and they satisfies the far-field of

$$\Phi_\varepsilon \rightarrow 0, \quad \Psi_\varepsilon \sim (\mathbf{a}^T \mathbf{e}) \frac{S_\varepsilon}{\rho^2}, \quad \text{as } \rho \rightarrow \infty.\tag{3.7}$$

The direction of oscillation of the spot at the onset of instability is determined by the value of \mathbf{a} . If \mathbf{a} is real, the spot oscillates through the equilibrium position along a line. However, if \mathbf{a} is complex, the motion exhibits rotation about the center. The value of $\mathbf{a}^T \mathbf{e}$ is obtained by matching with the outer solution.

In equation (3.7), the far-field behavior of Ψ_ε must match with the singular behavior of the leading order term of ψ in the outer region near the spot center, while the regular part of ψ must be matched by a constant term in the far-field of Ψ_2 .

Assume that $\tau \sim \mathcal{O}(\varepsilon^{-3})$, and $\lambda \sim \mathcal{O}(\varepsilon^2)$, thus $\tau\lambda \sim \mathcal{O}(\varepsilon^{-1})$ when τ is near the instability threshold. We scale τ and λ as

$$\lambda = \varepsilon^2 \lambda_0 + \varepsilon^3 \lambda_1, \quad \tau = \varepsilon^{-3} \tau_0 + \varepsilon^{-2} \tau_1.\tag{3.8}$$

At $\mathcal{O}(\varepsilon^2)$ in the inner region, we have

$$\Delta_{\mathbf{y}} \begin{pmatrix} \Phi_2 \\ \Psi_2 \end{pmatrix} + \mathcal{M} \begin{pmatrix} \Phi_2 \\ \Psi_2 \end{pmatrix} = \begin{pmatrix} \lambda_0 \Phi_\varepsilon \\ \frac{\tau_0 \lambda_0}{D} \Psi_\varepsilon \end{pmatrix}.\tag{3.9}$$

To analyze this system further, we begin by identifying the corresponding homogeneous solution to (3.9), which is readily found as

$$\Phi_{2h} = \kappa \partial_{S_\varepsilon} V_\varepsilon, \quad \Psi_{2h} = \kappa \partial_{S_\varepsilon} U_\varepsilon.\tag{3.10}$$

Here, κ is a scaling constant determined by matching the regular part of ψ at the spot location. Moving forward, we focus on the behavior of Ψ_2 as $\rho \rightarrow \infty$ by solving the following equivalent equation, which simplifies our analysis of the asymptotic behavior

$$\Delta_{\mathbf{y}} \Psi_{p2} = \frac{\mathbf{a}^T \mathbf{e} S_\varepsilon \tau_0 \lambda_0}{D \rho^2},\tag{3.11}$$

The solution to (3.11) is then given by

$$\Psi_{p2} = \mathbf{a}^T \mathbf{e} S_\varepsilon \frac{\lambda_0 \tau_0}{D} \left(-\frac{1}{2} + \frac{c_1}{\rho^2} + c_2 \rho \right).\tag{3.12}$$

Examining this solution, we note that the singular term of Ψ_{p2} is of order $\mathcal{O}(\varepsilon^4)$ in the outer region and can therefore be ignored. The $c_2 \rho_j$ term must match the $\mathcal{O}(\varepsilon)$ term in the outer region. However, since the leading order in the outer region should be $\mathcal{O}(\varepsilon^2)$, we impose $c_2 = 0$ to maintain consistency.

As a result, the far-field condition of Ψ_2 is given by

$$\Psi_2 \sim \kappa(\chi'(S_\varepsilon) - \frac{1}{\rho}) - \mathbf{a}^T \mathbf{e} S_\varepsilon \frac{\lambda_0 \tau_0}{2D}. \quad (3.13)$$

In the outer region, we expand $\psi \sim \varepsilon^2 \psi_1 + \varepsilon^3 \psi_2$. Thus ψ_1 satisfies

$$\begin{aligned} \Delta \psi_1 - \mu^2 \psi_1 &= 0, \quad \mathbf{x} \in \Omega; \quad \partial_n \psi_1 = 0, \quad \mathbf{x} \in \partial\Omega. \\ \psi_1 &\sim \frac{\mathbf{a}^T (\mathbf{x} - \mathbf{x}_1) S_\varepsilon}{|\mathbf{x} - \mathbf{x}_1|^3} + \kappa \chi'(S_\varepsilon) - \frac{\mathbf{a}^T (\mathbf{x} - \mathbf{x}_1) S_\varepsilon \mu^2}{2}, \quad \text{as } \mathbf{x} \rightarrow \mathbf{x}_1, \end{aligned} \quad (3.14)$$

where $\mu^2 = \frac{\tau_0 \lambda_0}{D}$. Therefore, we determine ψ_1 as

$$\psi_1 = -\frac{4\pi}{D} \left[S_\varepsilon \mathbf{a}^T \nabla_{\mathbf{x}_1} G_\mu(\mathbf{x}; \mathbf{x}_1) \right], \quad (3.15)$$

where $G_\mu(\mathbf{x}; \mathbf{x}_1)$ is the Helmholtz Green's function defined in (1.3), and $\nabla_{\mathbf{x}_1} G_\mu(\mathbf{x}; \mathbf{x}_1)$ is the gradient of $G_\mu(\mathbf{x}; \mathbf{x}_1)$ with respect to the second variable. The local behavior of $\nabla_{\mathbf{x}_1} G_\mu(\mathbf{x}; \mathbf{x}_1)$ near the spot is

$$\nabla_{\mathbf{x}_1} G_\mu(\mathbf{x}; \mathbf{x}_1) \sim -\frac{(\mathbf{x} - \mathbf{x}_1)}{4\pi |\mathbf{x} - \mathbf{x}_1|^3} + \mathbf{F}_\mu + (\mathbf{x} - \mathbf{x}_1) \cdot \mathcal{Q}_{\mu 1} + \frac{\mu^2 (\mathbf{x} - \mathbf{x}_1)}{8\pi |\mathbf{x} - \mathbf{x}_1|}, \quad \text{as } \mathbf{x} \rightarrow \mathbf{x}_1, \quad (3.16)$$

where we define the quantities

$$\mathbf{F}_\mu = \begin{pmatrix} F_\mu^{(1)} \\ F_\mu^{(2)} \\ F_\mu^{(3)} \end{pmatrix} = \nabla_{\mathbf{x}} R_\mu(\mathbf{x}; \mathbf{x}_1)|_{\mathbf{x}=\mathbf{x}_1}, \quad (3.17)$$

and $\mathcal{Q}_{\mu 1}$ is a 3×3 matrix computing by differentiating on $R_\mu(\mathbf{x}; \mathbf{x}_1)$ respect to the first variable, then differentiating each element of the resulting vector respect to the second variable, and lastly substitute $\mathbf{x} = \mathbf{x}_1$, yielding

$$\mathcal{Q}_{\mu 1} = \left(\nabla_{\mathbf{x}_1} \partial_{x_1} R_\mu(\mathbf{x}; \mathbf{x}_1) \quad \nabla_{\mathbf{x}_1} \partial_{x_2} R_\mu(\mathbf{x}; \mathbf{x}_1) \quad \nabla_{\mathbf{x}_1} \partial_{x_3} R_\mu(\mathbf{x}; \mathbf{x}_1) \right) \Big|_{\mathbf{x}=\mathbf{x}_1}. \quad (3.18)$$

At $\mathcal{O}(\varepsilon^3)$, ψ_2 satisfies

$$\begin{aligned} \Delta \psi_2 - \mu^2 \psi_2 &= \mu_1^2 \psi_1, \quad \mathbf{x} \in \Omega; \quad \partial_n \psi_2 = 0, \quad \mathbf{x} \in \partial\Omega. \\ \psi_2 &\sim -\frac{\kappa}{|\mathbf{x} - \mathbf{x}_1|}, \quad \text{as } \mathbf{x} \rightarrow \mathbf{x}_1, \end{aligned} \quad (3.19)$$

where $\mu_1^2 = \frac{\tau_0 \lambda_1 + \tau_1 \lambda_0}{D}$. We observed that the particular solution to (3.19) is the derivative of ψ_1 respect to μ^2 . Hence the expression of ψ_2 is

$$\psi_2 = \frac{4\pi}{D} \kappa G_\mu(\mathbf{x}; \mathbf{x}_1) + \mu_1^2 \partial_{\mu^2} \psi_1. \quad (3.20)$$

Now we generate the outer solution $\psi_\varepsilon = \psi_1 + \varepsilon \psi_2$ by adding (3.15) and (3.20), yielding

$$\psi_\varepsilon = -\frac{4\pi}{D} \left[S_\varepsilon \mathbf{a}^T \nabla_{\mathbf{x}_1} G_\mu(\mathbf{x}; \mathbf{x}_1) + \varepsilon \mu_1^2 S_\varepsilon \mathbf{a}^T \partial_{\mu^2} \nabla_{\mathbf{x}_1} G_\mu(\mathbf{x}; \mathbf{x}_1) - \varepsilon \kappa G_\mu(\mathbf{x}; \mathbf{x}_1) \right]. \quad (3.21)$$

We then match (3.21) with (3.7) and (3.13), using the local behavior of $G_\mu(\mathbf{x}; \mathbf{x}_1)$ and $\nabla_{\mathbf{x}_1} G_\mu(\mathbf{x}; \mathbf{x}_1)$ given in (1.3) and (3.16), to obtain the constants κ , which is

$$\kappa = -\frac{4\pi S_\varepsilon}{D \chi'(S_\varepsilon)} \mathbf{a}^T \nabla_{\mathbf{x}} R_\mu(\mathbf{x}; \mathbf{x}_1)|_{\mathbf{x}=\mathbf{x}_1}. \quad (3.22)$$

In highly symmetric geometries, such as a cube, sphere, or ellipsoid, the value of $\nabla_{\mathbf{x}} R_\mu(\mathbf{x}; \mathbf{x}_1)|_{\mathbf{x}=\mathbf{x}_1}$ coincides with $\nabla_{\mathbf{x}} R(\mathbf{x}; \mathbf{x}_1)|_{\mathbf{x}=\mathbf{x}_1}$, which is zero at equilibrium. Consequently, κ is zero according to (3.22).

To determine the Hopf stability threshold τ , the frequency of oscillations at onset λ , and the direction of oscillation of the spot \mathbf{a} , solvability conditions will be applied at $\mathcal{O}(\varepsilon^2)$ for Φ_2 and Ψ_2 , as well as at $\mathcal{O}(\varepsilon^3)$ for Φ_3 and Ψ_3 . In the following analysis, we combine the results of the $\mathcal{O}(\varepsilon^2)$ and $\mathcal{O}(\varepsilon^3)$ analyses in the inner region to obtain

$$\Delta_{\mathbf{y}} \mathbf{W}_1 + \mathcal{M} \mathbf{W}_1 = \begin{pmatrix} (\lambda_0 + \varepsilon \lambda_1) \Phi_\varepsilon \\ \mu_\varepsilon^2 \Psi_\varepsilon \end{pmatrix} + \varepsilon \mathcal{N} \begin{pmatrix} \Phi_\varepsilon \\ \Psi_\varepsilon \end{pmatrix}, \quad (3.23)$$

where

$$\mathbf{W}_1 = \begin{pmatrix} \Phi_2 + \varepsilon\Phi_3 \\ \Psi_2 + \varepsilon\Psi_3 \end{pmatrix}, \quad \mathcal{N} = \begin{pmatrix} -2V_\varepsilon U_3 - 2V_3 U_\varepsilon & -2V_\varepsilon V_3 \\ 2V_\varepsilon U_3 + 2V_3 U_\varepsilon & 2V_\varepsilon V_3 \end{pmatrix}, \quad \mu_\varepsilon = \mu + \varepsilon\mu_1. \quad (3.24)$$

According to (1.3) and (3.16), expanding (3.21) yields the far-field behavior of \mathbf{W}_1 as $\rho \rightarrow \infty$, namely

$$\mathbf{W}_1 \sim \begin{pmatrix} 0 \\ -\frac{4\pi}{D} \left[S_\varepsilon \mathbf{a}^T (\varepsilon \mathcal{Q}_{\mu_1} \rho + \frac{\mu_\varepsilon^2}{8\pi}) \mathbf{e} - \kappa (\chi'(S_\varepsilon) - \frac{1}{\rho}) - \varepsilon \kappa R_\mu(\mathbf{x}_1; \mathbf{x}_1) \right] \end{pmatrix}. \quad (3.25)$$

Next, we apply solvability conditions on (3.23). The vector \mathbf{W}_1 can be decomposed into four components as

$$\mathbf{W}_1 = \mathbf{W}_{sc} \sin \theta \cos \varphi + \mathbf{W}_{ss} \sin \theta \sin \varphi + \mathbf{W}_{cc} \cos \theta + \bar{\mathbf{W}}, \quad (3.26)$$

where $\mathbf{W}_{sc}, \mathbf{W}_{ss}, \mathbf{W}_{cc}$ and $\bar{\mathbf{W}}$ are 2×1 vectors satisfying

$$\begin{aligned} \Delta_{11} \mathbf{W}_{sc} - \mathcal{M} \mathbf{W}_{sc} &= a_1 \begin{bmatrix} (\lambda_0 + \varepsilon\lambda_1) \partial_\rho V_\varepsilon \\ \mu_\varepsilon^2 \partial_\rho U_\varepsilon \end{bmatrix}, & \Delta_{11} \mathbf{W}_{ss} - \mathcal{M} \mathbf{W}_{ss} &= a_2 \begin{bmatrix} (\lambda_0 + \varepsilon\lambda_1) \partial_\rho V_\varepsilon \\ \mu_\varepsilon^2 \partial_\rho U_\varepsilon \end{bmatrix}, \\ \Delta_{11} \mathbf{W}_{cc} - \mathcal{M} \mathbf{W}_{cc} &= a_3 \begin{bmatrix} (\lambda_0 + \varepsilon\lambda_1) \partial_\rho V_\varepsilon \\ \mu_\varepsilon^2 \partial_\rho U_\varepsilon \end{bmatrix}, & \Delta_\rho \bar{\mathbf{W}} - \mathcal{M} \bar{\mathbf{W}} &= \mathbf{0}, \end{aligned} \quad (3.27)$$

with far-field conditions

$$\begin{aligned} \mathbf{W}_{sc} &\sim \begin{pmatrix} 0 \\ -\frac{4\pi}{D} \varepsilon S_\varepsilon a_{Q1} \rho - \frac{a_1 S_\varepsilon \mu_\varepsilon^2}{2} \end{pmatrix}, & \mathbf{W}_{ss} &\sim \begin{pmatrix} 0 \\ -\frac{4\pi}{D} \varepsilon S_\varepsilon a_{Q2} \rho - \frac{a_2 S_\varepsilon \mu_\varepsilon^2}{2} \end{pmatrix}, \\ \mathbf{W}_{cc} &\sim \begin{pmatrix} 0 \\ \frac{4\pi}{D} \varepsilon S_\varepsilon a_{Q3} \rho - \frac{a_3 S_\varepsilon \mu_\varepsilon^2}{2} \end{pmatrix}, & \bar{\mathbf{W}} &\sim \begin{pmatrix} 0 \\ -\frac{4\pi}{D} \left[\kappa (\chi'(S_\varepsilon) - \frac{1}{\rho}) + \varepsilon \kappa R_\mu(\mathbf{x}_1; \mathbf{x}_1) \right] \end{pmatrix}. \end{aligned} \quad (3.28)$$

Here $\Delta_{11} = \partial_{\rho\rho} + 2\rho^{-1}\partial_\rho - 2\rho^{-2}$ is the translation mode, and $\mathcal{Q}_\mu^T \mathbf{a} = (a_{Q1}, a_{Q2}, a_{Q3})^T$.

The non-homogeneous terms of (3.23) must be orthogonal to the null space of the homogeneous adjoint operation, given by

$$\Delta_\mathbf{y} \mathbf{P} + \mathcal{M}^T \mathbf{P} = \mathbf{0}, \quad \mathbf{y} \in \mathbb{R}^3. \quad (3.29)$$

Similarly, we seek three linearly independent solutions of the form $\mathbf{P}_{sc} = \bar{\mathbf{P}} \sin \theta \cos \varphi$, $\mathbf{P}_{ss} = \bar{\mathbf{P}} \sin \theta \sin \varphi$, $\mathbf{P}_{cc} = \bar{\mathbf{P}} \cos \theta$, and the radially symmetric $\bar{\mathbf{P}}$ satisfies

$$\Delta_1 \bar{\mathbf{P}} + \mathcal{M}^T \bar{\mathbf{P}} = \mathbf{0}, \quad \bar{\mathbf{P}} = \begin{pmatrix} \bar{P}_1 \\ \bar{P}_2 \end{pmatrix} \quad (3.30)$$

with boundary and far-field conditions

$$\bar{\mathbf{P}}(\mathbf{0}) = \mathbf{0}, \quad \bar{\mathbf{P}} \sim \begin{pmatrix} 0 \\ 1/\rho^2 \end{pmatrix}, \quad \text{as } \rho \rightarrow \infty. \quad (3.31)$$

To apply the solvability condition, we multiply (3.23) by $\mathbf{P}_{sc,ss,cc}$ on the left, respectively, and integrate over a ball with radius $R \gg 1$ centered at the origin, so we obtain

$$\begin{aligned} & \int \int \int_{B_R} \mathbf{P}_{sc,ss,cc}^T [\Delta_\mathbf{y} \mathbf{W}_1 + \mathcal{M} \mathbf{W}_1] d\mathbf{y} \\ &= \int \int \int_{B_R} \mathbf{P}_{sc,ss,cc}^T \left[\begin{pmatrix} (\lambda_0 + \varepsilon\lambda_1) \Phi_\varepsilon \\ \mu_\varepsilon^2 \Psi_\varepsilon \end{pmatrix} + \mathcal{N} \begin{pmatrix} \Phi_\varepsilon \\ \Psi_\varepsilon \end{pmatrix} \right] d\mathbf{y}. \end{aligned} \quad (3.32)$$

We now compute each term in (3.32). On the left, we use Green's identity to obtain

$$\begin{aligned} & \int \int \int_{B_R} \mathbf{P}_{sc,ss,cc}^T [\Delta_{\mathbf{y}_1} \mathbf{W}_1 + \mathcal{M} \mathbf{W}_1] d\mathbf{y}_1 \\ &= \int_0^\pi \int_0^{2\pi} (\mathbf{P}_{sc,ss,cc}^T \partial_\rho \mathbf{W}_1 + \mathbf{W}_1^T \partial_\rho \mathbf{P}_{sc,ss,cc}) \rho^2|_{\rho=R} \sin \theta_1 d\varphi_1 d\theta_1. \end{aligned} \quad (3.33)$$

Therefore, with the far-field in (3.28), (3.29) and (3.31), we get

$$\begin{aligned}
\int_0^\pi \int_0^{2\pi} \mathbf{P}_{sc}^T \partial_\rho \mathbf{W}_1 + \mathbf{W}_1^T \partial_\rho \mathbf{P}_{sc} \rho^2|_{\rho=R} \sin \theta_1 d\varphi_1 d\theta_1 &\sim -\frac{\varepsilon 16\pi^2 S_\varepsilon a_{Q1}}{D} - \frac{4\pi}{3} \frac{a_1 S_\varepsilon \mu_\varepsilon^2}{R}, \\
\int_0^\pi \int_0^{2\pi} \mathbf{P}_{ss}^T \partial_\rho \mathbf{W}_1 + \mathbf{W}_1^T \partial_\rho \mathbf{P}_{ss} \rho^2|_{\rho=R} \sin \theta_1 d\varphi_1 d\theta_1 &\sim -\frac{\varepsilon 16\pi^2 S_\varepsilon a_{Q2}}{D} - \frac{4\pi}{3} \frac{a_2 S_\varepsilon \mu_\varepsilon^2}{R}, \\
\int_0^\pi \int_0^{2\pi} \mathbf{P}_{cc}^T \partial_\rho \mathbf{W}_1 + \mathbf{W}_1^T \partial_\rho \mathbf{P}_{cc} \rho^2|_{\rho=R} \sin \theta_1 d\varphi_1 d\theta_1 &\sim -\frac{\varepsilon 16\pi^2 S_\varepsilon a_{Q3}}{D} - \frac{4\pi}{3} \frac{a_3 S_\varepsilon \mu_\varepsilon^2}{R}.
\end{aligned} \tag{3.34}$$

On the right-hand side of (3.104), we apply integration by parts on the first term, and use (3.6) to obtain

$$\begin{aligned}
\iiint_{B_R} \mathbf{P}_{sc}^T \begin{pmatrix} (\lambda_0 + \varepsilon\lambda_1)\Phi_\varepsilon \\ \mu_\varepsilon^2 \Psi_\varepsilon \end{pmatrix} d\mathbf{y}_1 &\sim \frac{4\pi a_1}{3} \left((\lambda_0 + \varepsilon\lambda_1)k_1 - \mu_\varepsilon^2 k_2 - \frac{\mu_\varepsilon^2 S_\varepsilon}{R} \right), \\
\iiint_{B_R} \mathbf{P}_{ss}^T \begin{pmatrix} (\lambda_0 + \varepsilon\lambda_1)\Phi_\varepsilon \\ \mu_\varepsilon^2 \Psi_\varepsilon \end{pmatrix} d\mathbf{y}_1 &\sim \frac{4\pi a_2}{3} \left((\lambda_0 + \varepsilon\lambda_1)k_1 - \mu_\varepsilon^2 k_2 - \frac{\mu_\varepsilon^2 S_\varepsilon}{R} \right), \\
\iiint_{B_R} \mathbf{P}_{cc}^T \begin{pmatrix} (\lambda_0 + \varepsilon\lambda_1)\Phi_\varepsilon \\ \mu_\varepsilon^2 \Psi_\varepsilon \end{pmatrix} d\mathbf{y}_1 &\sim \frac{4\pi a_3}{3} \left((\lambda_0 + \varepsilon\lambda_1)k_1 - \mu_\varepsilon^2 k_2 - \frac{\mu_\varepsilon^2 S_\varepsilon}{R} \right),
\end{aligned} \tag{3.35}$$

where k_1 and k_2 are defined by the integrals

$$k_1 = \int_0^\infty V_{\varepsilon 1}' \bar{P}_1 \rho^2 d\rho, \quad k_2 = \int_0^\infty [U_\varepsilon - \chi(S_\varepsilon)] (\bar{P}_2 \rho^2)' d\rho. \tag{3.36}$$

We plot the value of k_1 and k_2 versus S_ε in Figure 3.

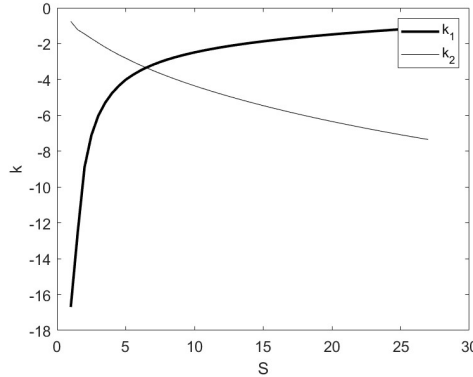


Figure 3: A plot of k_1 and k_2 versus S_ε as defined in (3.36).

For the last term of the right side of (3.104), we use (3.6) to compute

$$\mathcal{N} \begin{pmatrix} \Phi_\varepsilon \\ \Psi_\varepsilon \end{pmatrix} = \mathcal{N} \mathbf{a}_1 \cdot \nabla_{\mathbf{y}_1} \begin{pmatrix} V_\varepsilon \\ U_\varepsilon \end{pmatrix}. \tag{3.37}$$

Expanding (3.37), we have

$$\mathcal{N} \begin{pmatrix} \Phi_\varepsilon \\ \Psi_\varepsilon \end{pmatrix} = \begin{pmatrix} -U_3 \mathbf{a}_1 \cdot \nabla_{\mathbf{y}_1} V_\varepsilon^2 - V_3 \mathbf{a}_1 \cdot \nabla_{\mathbf{y}_1} (2V_\varepsilon U_\varepsilon) \\ U_3 \mathbf{a}_1 \cdot \nabla_{\mathbf{y}_1} V_\varepsilon^2 + V_3 \mathbf{a}_1 \cdot \nabla_{\mathbf{y}_1} (2V_\varepsilon U_\varepsilon) \end{pmatrix}. \tag{3.38}$$

By constructing full derivatives, and passing the operator $\mathbf{a}_1 \cdot \nabla_{\mathbf{y}_1}$, we find

$$\mathcal{N} \begin{pmatrix} \Phi_\varepsilon \\ \Psi_\varepsilon \end{pmatrix} = \begin{pmatrix} -\mathbf{a}_1 \cdot \nabla_{\mathbf{y}_1} (V_\varepsilon^2 U_3 + 2U_\varepsilon V_\varepsilon V_3) + V_\varepsilon^2 \mathbf{a}_1 \cdot \nabla_{\mathbf{y}_1} U_3 + 2U_\varepsilon V_\varepsilon \mathbf{a}_1 \cdot \nabla_{\mathbf{y}_1} V_3 \\ \mathbf{a}_1 \cdot \nabla_{\mathbf{y}_1} (V_\varepsilon^2 U_3 + 2U_\varepsilon V_\varepsilon V_3) - V_\varepsilon^2 \mathbf{a}_1 \cdot \nabla_{\mathbf{y}_1} U_3 - 2U_\varepsilon V_\varepsilon \mathbf{a}_1 \cdot \nabla_{\mathbf{y}_1} V_3 \end{pmatrix}. \tag{3.39}$$

From (2.12), we observe that

$$\begin{aligned} -\mathbf{a}_1 \cdot \nabla_{\mathbf{y}_1} (V_\varepsilon^2 U_3 + 2U_\varepsilon V_\varepsilon V_3) &= \Delta_{\mathbf{y}_1} \mathbf{a}_1 \cdot \nabla_{\mathbf{y}_1} V_3 - \mathbf{a}_1 \cdot \nabla_{\mathbf{y}_1} V_3, \\ \mathbf{a}_1 \cdot \nabla_{\mathbf{y}_1} (V_\varepsilon^2 U_3 + 2U_\varepsilon V_\varepsilon V_3) &= \Delta_{\mathbf{y}_1} \mathbf{a}_1 \cdot \nabla_{\mathbf{y}_1} U_3. \end{aligned} \quad (3.40)$$

Hence we have

$$\begin{aligned} \mathcal{N} \begin{pmatrix} \Phi_\varepsilon \\ \Psi_\varepsilon \end{pmatrix} &= [\Delta_{\mathbf{y}_1} + \mathcal{M}] (\mathbf{a}_1 \cdot \nabla_{\mathbf{y}_1}) \mathbf{n}; \quad \mathbf{n} = \begin{pmatrix} V_3 \\ U_3 \end{pmatrix}, \\ \mathbf{a}_1 \cdot \nabla_{\mathbf{y}_1} \mathbf{n} &\sim \begin{pmatrix} 0 \\ -4\pi \mathbf{a}^T S_\varepsilon \mathcal{H}_{11} \mathbf{e}_\rho \end{pmatrix}, \quad \text{as } \rho \rightarrow \infty. \end{aligned} \quad (3.41)$$

Multiplying (3.41) by $\mathbf{P}_{sc,ss,cc}^T$ and applying the divergence theorem, we get

$$\iint \int_{B_R} \mathbf{P}_{sc,ss,cc}^T \mathcal{N} \begin{pmatrix} \Phi_\varepsilon \\ \Psi_\varepsilon \end{pmatrix} d\mathbf{y}_1 \sim -16\pi^2 S_\varepsilon \left(a_1 \mathcal{H}_{11}^{(1n)} + a_2 \mathcal{H}_{11}^{(2n)} + a_3 \mathcal{H}_{11}^{(3n)} \right), \quad n = 1, 2, 3, \quad (3.42)$$

where $\mathcal{H}_{ji}^{(mn)}$ is the (m, n) th entry of \mathcal{H}_{ji} .

Now we substitute (3.34), (3.35) and (3.42) to (3.32) with $R \gg 1$ and cancel the term of $1/R$, yielding

$$-\frac{\varepsilon 16\pi^2 S_\varepsilon a_{Qn}}{D} = \frac{4\pi a_n}{3} \left((\lambda_0 + \varepsilon \lambda_1) k_1 - \mu_\varepsilon^2 k_2 \right) - 16\varepsilon \pi^2 S_\varepsilon \left(a_1 \mathcal{H}_{11}^{(1n)} + a_2 \mathcal{H}_{11}^{(2n)} + a_3 \mathcal{H}_{11}^{(3n)} \right), \quad n = 1, 2, 3, \quad (3.43)$$

To obtain the leading order of τ , we collect the leading order terms from (3.43) and use $\mu_\varepsilon^2 = \frac{1}{D} (\tau_0 \lambda_0 + \varepsilon (\tau_0 \lambda_1 + \tau_1 \lambda_0))$ to have

$$(k_2 \tau_0 - D k_1) \lambda_0 = 0, \quad (3.44)$$

where k_1 and k_2 are defined in (3.36). Assuming λ_0 is nonzero in (3.8), we obtain the leading order threshold is given by

$$\tau_0 = \frac{D k_1}{k_2}, \quad (3.45)$$

Similarly, by collecting $\mathcal{O}(\varepsilon)$ terms from (3.43), we get

$$-\frac{16\pi^2 S_\varepsilon a_{Qn}}{D} = \frac{4\pi a_n}{3} (\lambda_1 k_1 - (\tau_0 \lambda_1 + \tau_1 \lambda_0) k_2) - 16\pi^2 S_\varepsilon \left(a_1 \mathcal{H}_{11}^{(1n)} + a_2 \mathcal{H}_{11}^{(2n)} + a_3 \mathcal{H}_{11}^{(3n)} \right), \quad n = 1, 2, 3, \quad (3.46)$$

By (3.45), we further simplify (3.46) to

$$\frac{12\pi S_\varepsilon a_{Qn}}{D} = a_n \tau_1 \lambda_0 k_2 + 12\pi S_\varepsilon \left(a_1 \mathcal{H}_{11}^{(1n)} + a_2 \mathcal{H}_{11}^{(2n)} + a_3 \mathcal{H}_{11}^{(3n)} \right), \quad n = 1, 2, 3, \quad (3.47)$$

Substituting a_{Q_i} , we arrive at a 3×3 matrix-eigenvalue problem for the oscillation modes \mathbf{a} , Hopf bifurcation frequency λ_0 and the first correction of the threshold τ_1 ,

$$\frac{12\pi}{\tau_1 k_2} [S_\varepsilon (\mathcal{Q}_{\mu 1} - D \mathcal{H}_{11})^T] \mathbf{a} = \lambda_0 \mathbf{a}, \quad (3.48)$$

where $\mathcal{Q}_{\mu 1}$ is defined in (3.18), and \mathcal{H}_{11} is given in (2.12). As shown in the matrix eigenvalue problem, the value of κ does not contribute to the computation of solvability or to calculating the Hopf bifurcation (HB) threshold. Therefore, in the following analysis, we will not calculate the value of κ .

To determine the threshold of τ beyond which translatory oscillatory instability is triggered, we set $\lambda_0 = \lambda_I i$ and $\mu_I^2 = \tau_0 \lambda_I i$. By solving two transcendental equations, namely

$$\begin{aligned} \mathbf{Re} \left\{ \det \left(\frac{12\pi}{\tau_1 k_2} [S_\varepsilon (\mathcal{Q}_{\mu 1} - \mathcal{H}_{11})^T - S_{\varepsilon 0} \mathcal{H}_{10}^T] - \lambda_I i \mathcal{I}_3 \right) \right\} &= 0, \\ \mathbf{Im} \left\{ \det \left(\frac{12\pi}{\tau_1 k_2} [S_\varepsilon (\mathcal{Q}_{\mu 1} - \mathcal{H}_{11})^T - S_{\varepsilon 0} \mathcal{H}_{10}^T] - \lambda_I i \mathcal{I}_3 \right) \right\} &= 0, \end{aligned} \quad (3.49)$$

we obtain the critical value τ_1^* and the corresponding eigenvalue λ_I^* . Together with (3.45), we thus conclude that $\tau^* = \tau_0^* + \varepsilon \tau_1^*$.

As τ increases beyond τ^* , the real part of the dominant complex eigenvalue crosses the imaginary axis from left to right, entering the positive side and triggering translational oscillatory instability. In an asymmetric geometry, multiple solutions may be found in the system (3.49), each corresponding to a distinct oscillation mode with frequency $2\pi/\lambda_I^*$. However, the leading order Hopf bifurcation value τ_0^* , governed by the source strength of the spot $S\varepsilon$, remains the same across different oscillation modes. Thus, the preferred oscillatory mode is determined by the first-order correction τ_1^* . The minimum τ^* among all possible values represents the Hopf stability threshold, with the corresponding null space \mathbf{a}^* of the matrix in (3.49) indicating the direction of spot oscillation at onset

In this section, we examine the problem on various types of domains, including a unit sphere, a perturbed sphere, and a defected sphere. The purpose of this section is to investigate how geometry affects the preferred direction of oscillation at onset.

3.1 The unit sphere

In an unit sphere, the matrices $Q_{\mu 1}$ and \mathcal{H}_{11} are diagonal and can be expressed as a constant times an identity matrix. Therefore, the eigenvalue system (3.48) can be simplified to

$$12\pi S\varepsilon \left(Q_{\mu 1}^{(1,1)} - D\mathcal{H}_{11}^{(1,1)} \right) - k_2 \tau_1 \lambda_I = 0. \quad (3.50)$$

In this case, the vector \mathbf{a} , which indicates the direction of spot oscillation at onset, becomes arbitrary, and there is no preferred direction of oscillation.

We now solve the equation (3.50). We first need $Q_{\mu 1}$, the gradient with respect to the source location of the regular part of the Helmholtz Green's function, and the Hessian matrix of the Neumann Green's function \mathcal{H}_{11} .

We begin by computing $Q_{\mu 1}$. Rather than solving the Helmholtz Green's function on a unit sphere and then differentiating with respect to the source location, we directly solve PDE of the gradient of the Helmholtz Green's function. Let $\mathbf{g}_0 = \nabla_{\mathbf{x}_1} G_\mu(\mathbf{x}; \mathbf{x}_1)$, which satisfies

$$\begin{aligned} \Delta \mathbf{g}_0 - \mu^2 \mathbf{g}_0 &= \nabla_{\mathbf{x}_1} \delta(\mathbf{x} - \mathbf{x}_1), \quad \mathbf{x} \in \Omega; \quad \partial_n \mathbf{g}_0 = \mathbf{0}, \quad \mathbf{x} \in \partial\Omega; \\ \mathbf{g}_0 &\sim -\frac{(\mathbf{x} - \mathbf{x}_1)}{4\pi|\mathbf{x} - \mathbf{x}_1|^3} + \nabla_{\mathbf{x}_1} R_\mu(\mathbf{x}; \mathbf{x}_1) + \frac{\mu^2 (\mathbf{x} - \mathbf{x}_1)}{8\pi |\mathbf{x} - \mathbf{x}_1|}, \quad \text{as } \mathbf{x} \rightarrow \mathbf{x}_1. \end{aligned} \quad (3.51)$$

We highlight that \mathbf{g}_0 is a 3×1 vector, so its far-field behavior of \mathbf{g}_0 contains three components. The explicit solution is

$$\mathbf{g}_0 = -\left(\frac{\mu}{2\pi}\right)^{\frac{3}{2}} F(r) \mathbf{e}, \quad F(r) = r^{-\frac{1}{2}} \left(Q(\mu) I_{\frac{3}{2}}(\mu r) + K_{\frac{3}{2}}(\mu r) \right), \quad (3.52)$$

where $r = |\mathbf{x} - \mathbf{x}_1|$, \mathbf{e} is defined in (2.1), $I_n(z)$ and $K_n(z)$ are the modified Bessel functions

$$Q(\mu) = -\frac{2\mu K'_{3/2}(\mu) - K_{3/2}(\mu)}{2\mu I'_{3/2}(\mu) - I_{3/2}(\mu)}. \quad (3.53)$$

Using $\nabla_{\mathbf{x}} = \mathbf{e} \partial_r + \frac{1}{r \sin^2 \theta} \mathbf{e}_\varphi \partial_\varphi + \frac{1}{r} \mathbf{e}_\theta \partial_\theta$ with

$$\mathbf{e}_\varphi = \begin{pmatrix} -\sin \theta \sin \varphi \\ \sin \theta \cos \varphi \\ 0 \end{pmatrix}, \quad \mathbf{e}_\theta = \begin{pmatrix} \cos \theta \cos \varphi \\ \cos \theta \sin \varphi \\ -\sin \theta \end{pmatrix}, \quad (3.54)$$

and setting $\mathbf{x} = \mathbf{x}_1$, we obtain

$$\begin{aligned} \nabla_{\mathbf{x}} g_0^{(1)}|_{\mathbf{x}=\mathbf{x}_1} &= -\left(\frac{\mu}{2\pi}\right)^{\frac{3}{2}} \left[F'(r_0) \sin \theta_0 \cos \varphi_0 \mathbf{e}_0 - \frac{1}{r_0 \sin^2 \theta_0} F(r_0) \sin \theta_0 \sin \varphi_0 \mathbf{e}_{\varphi_0} \right. \\ &\quad \left. + \frac{1}{r_0} F(r_0) \cos \theta_0 \cos \varphi_0 \mathbf{e}_{\theta_0} \right]. \end{aligned} \quad (3.55)$$

From the fact that for a small argument, $|z| \ll 1$,

$$\begin{aligned} I_{\frac{3}{2}}(z) z^{-\frac{1}{2}} &\sim \frac{1}{3} \sqrt{\frac{2}{\pi}} z + \mathcal{O}(z^3), \\ K_{\frac{3}{2}}(z) z^{-\frac{1}{2}} &\sim \sqrt{\frac{\pi}{2}} z^{-2} - \frac{1}{2} \sqrt{\frac{\pi}{2}} + \frac{1}{3} \sqrt{\frac{\pi}{2}} z + \mathcal{O}(z^2), \end{aligned} \quad (3.56)$$

we find

$$\begin{aligned}\lim_{r \rightarrow 0^+} F'(r) &= -\frac{\sqrt{2\pi}}{\mu^{3/2}r^3} + \frac{(\pi + 2Q(\mu))\mu^{3/2}}{3\sqrt{2\pi}}, \\ \lim_{r \rightarrow 0^+} F(r)/r &= \sqrt{\frac{\pi}{2}} \frac{1}{\mu^{3/2}r^3} - \sqrt{\frac{\pi\mu}{2}} \frac{1}{2r} + \frac{(\pi + 2Q(\mu))\mu^{3/2}}{3\sqrt{2\pi}}.\end{aligned}\tag{3.57}$$

Recalling that $\mathcal{Q}_{\mu 1}$ is computed from the regular part of $G_{\mu}(\mathbf{x}; \mathbf{x}_1)$, we extract the regular part from (3.57) and substitute into (3.55), yielding the first column of $\mathcal{Q}_{\mu 1}$,

$$\begin{pmatrix} \mathcal{Q}_{\mu 1}^{(1,1)} \\ \mathcal{Q}_{\mu 1}^{(2,1)} \\ \mathcal{Q}_{\mu 1}^{(3,1)} \end{pmatrix} = -\frac{(\pi + 2Q(\mu))\mu^3}{12\pi^2} \begin{pmatrix} 1 \\ 0 \\ 0 \end{pmatrix}.\tag{3.58}$$

As expected, the second and third elements of the first column are zero, indicating the diagonal structure of $\mathcal{Q}_{\mu 1}$ due to the symmetric properties of a unit sphere. The similar results hold when computing the second and third columns of $\mathcal{Q}_{\mu 1}$.

The Neumann Green's function $G(r)$ satisfying (2.8) with source at the origin is given by

$$G(r) = \frac{1}{4\pi r} + \frac{r^2}{8\pi} - \frac{9}{20\pi}.\tag{3.59}$$

Thus the Hessian term is $\mathcal{H}_{11}^{(1,1)} = \frac{1}{4\pi}$.

From (3.58) and using $\mathcal{H}_{11}^{(1,1)} = (4\pi)^{-1}$, we derive, from (3.50),

$$12\pi S_{\varepsilon} \left(-\frac{(\pi + 2Q(\mu))\mu^3}{12\pi^2} - \frac{D}{4\pi} \right) - k_2\tau_1\lambda_I = 0.\tag{3.60}$$

By solving (3.60), we obtain τ_1 and the corresponding leading-order eigenvalue λ_I . We plot τ_1 and λ_I as functions of the feed rate A in Figure 4. As shown in (4a), the value of τ_1 monotonically approaches zero as A increases. Hence, as A becomes large, the value of τ_1 is too small to contribute as a correction term. Therefore, we compute the next-order correction, $\mathcal{O}(\varepsilon^2)$, for τ .

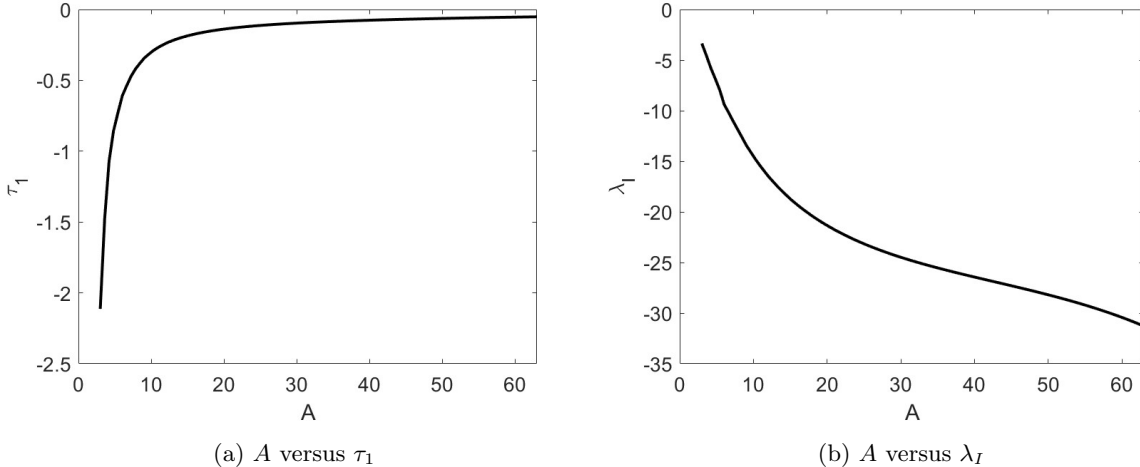


Figure 4: (a) First order correction of Hopf bifurcation threshold and (b) the leading order of the corresponding eigenvalue obtained by solving (3.60). τ_1 is approaching zero as A increase. λ_I is the pure imaginary eigenvalue.

Let $\tau = \varepsilon^{-3}(\tau_0 + \varepsilon\tau_1 + \varepsilon^2\tau_2)$ and $\lambda = \varepsilon^2(\lambda_0 + \varepsilon\lambda_1 + \varepsilon^2\lambda_2)$. We now aim to derive an eigenvalue system similar to (3.48) in Section 3. The process of computing τ_2 and λ_1 follows that in Section 3, therefore, we focus only on the differences in the following analysis.

In the outer region, we expand $\psi \sim \varepsilon^2 \psi_1 + \varepsilon^3 \psi_2 + \varepsilon^4 \psi_3$, where ψ_3 satisfies

$$\Delta \psi_3 - \mu^2 \psi_3 = \mu_1^2 \psi_2 + (\tau_0 \lambda_2 + \tau_1 \lambda_1 + \tau_2 \lambda_0) \psi_1, \quad \mathbf{x} \in \Omega; \quad \partial_n \psi_3 = 0, \mathbf{x} \in \partial\Omega. \quad (3.61)$$

In a unit ball, we let

$$\psi_i = \mathbf{a}^T \mathbf{e} \tilde{\psi}_i(r), \quad r = |\mathbf{x} - \mathbf{x}_1|, \quad i = 1, 2, 3, \quad (3.62)$$

so that (3.61) simplifies to

$$\Delta_{11} \tilde{\psi}_3 - \mu^2 \tilde{\psi}_3 = \mu_1^2 \tilde{\psi}_2 + \frac{\tau_0 \lambda_2 + \tau_1 \lambda_1 + \tau_2 \lambda_0}{D} \tilde{\psi}_1, \quad (3.63)$$

where $\Delta_{11} = \partial_{\rho\rho} + 2\rho^{-1} \partial_\rho - 2\rho^{-2}$. We solve (3.63) to find

$$\tilde{\psi}_3 \sim \frac{1}{r^2} \left[h_1 e^{\mu r} (\mu r - 1) + h_2 e^{-\mu r} (\mu r + 1) \right] + \frac{\tau_0 \lambda_2 + \tau_1 \lambda_1 + \tau_2 \lambda_0}{2D} \left[h_3 e^{\mu r} - h_4 e^{-\mu r} \right] + \mathcal{O}(r), \quad (3.64)$$

where $h_3 = 1/(Q(\mu) - 1)$, $h_4 = Q(\mu)/(Q(\mu) - 1)$, and $Q(\mu)$ is defined in (3.53). Thus, the local behavior of $\tilde{\psi}_3$ is

$$\tilde{\psi}_3 \sim \frac{h_1 - h_2}{r^2} + \frac{\tau_0 \lambda_2 + \tau_1 \lambda_1 + \tau_2 \lambda_0}{2D} (h_3 - h_4) - \frac{\mu^2}{2} (h_2 - h_1). \quad (3.65)$$

The first term in (3.65) matches the singular term of Ψ_2 in the inner region, as described in Section 3, while the second term matches Ψ_4 in the inner region. The last term in (3.65) corresponds to the $\mathcal{O}(\varepsilon)$ term in the inner region, which combines with $\mathcal{O}(1)$ terms to form Ψ_ε . However, in a single-spot pattern, the $\mathcal{O}(\varepsilon)$ term is actually zero because U_1 is zero according to [17], and Ψ_1 is derived from the partial derivative of U_1 . This results in $h_1 = h_2$, causing the last term to vanish, as well as the singular term in (3.65).

Using the local behavior of ψ_ε in (3.21) and $\tilde{\psi}_3$ in (3.65), we derive the far-field behavior of Ψ_4 in the inner region, yielding

$$\Psi_4 \sim \mathbf{a}^T \mathbf{e} S_\varepsilon \left\{ -\frac{1}{8} \mu^4 \rho^2 + \frac{2d_1}{3} \rho + \frac{\mu \mu_1^2}{2} (h_3 + h_4) \rho - \frac{\tau_0 \lambda_2 + \tau_1 \lambda_1 + \tau_2 \lambda_0}{2D} \right\}, \quad \text{as } \rho \rightarrow \infty, \quad (3.66)$$

where $d_1 = -\frac{e^{2\mu} \mu_1^2 (\mu^6 + 2\mu^4)}{(2+2\mu+\mu^2 - e^{2\mu}(2-2\mu+\mu^2))^2}$. In the inner region of $\mathcal{O}(\varepsilon^4)$, Φ_4 and Ψ_4 satisfy

$$\Delta_{\mathbf{y}} \begin{pmatrix} \Phi_4 \\ \Psi_4 \end{pmatrix} + \mathcal{M} \begin{pmatrix} \Phi_4 \\ \Psi_4 \end{pmatrix} = \mathcal{N}_1 \begin{pmatrix} \Phi_\varepsilon \\ \Psi_\varepsilon \end{pmatrix} + \begin{pmatrix} \lambda_2 \Phi_\varepsilon + \lambda_0 \Phi_2 \\ \frac{\tau_0 \lambda_2 + \tau_1 \lambda_1 + \tau_2 \lambda_0}{D} \Psi_\varepsilon + \mu^2 \Psi_2 \end{pmatrix}. \quad (3.67)$$

Here \mathcal{N}_1 is

$$\mathcal{N}_1 = \begin{pmatrix} 2U_4 V_\varepsilon + 2U_\varepsilon V_4 & 2V_\varepsilon V_4 \\ -2U_4 V_\varepsilon - 2U_\varepsilon V_4 & -2V_\varepsilon V_4 \end{pmatrix}, \quad (3.68)$$

where V_4 and U_4 are the $\mathcal{O}(\varepsilon^4)$ correction to the equilibrium solution in the inner region, satisfying

$$\begin{aligned} \Delta_{\mathbf{y}} \begin{pmatrix} V_4 \\ U_4 \end{pmatrix} + \mathcal{M} \begin{pmatrix} V_4 \\ U_4 \end{pmatrix} &= \mathbf{0}, \\ V_4 &\rightarrow 0, \quad U_4 \rightarrow c_3 - \frac{c_4}{\rho}, \quad \text{as } \rho \rightarrow 0. \end{aligned} \quad (3.69)$$

Here, c_3 and c_4 are constants obtained by matching to the outer solution. However, When applying the solvability conditions to (3.67), we compute $\mathbf{a} \cdot \nabla_{\mathbf{y}} U_4$, following the process from (3.37) to (3.42), which causes the constant c_3 to disappear. Additionally, the singular term in the far-field of U_4 must be balanced by other terms in the solvability conditions, so we do not need to compute c_4 either.

Now we apply the solvability conditions on (3.67). We multiply (3.67) by $\mathbf{P}_{sc,ss,cc}$ on both side and integrate over a large ball, yielding

$$\begin{aligned} \int \int \int_{R_B} \mathbf{P}_{sc,ss,cc}^T \left(\Delta_{\mathbf{y}} \begin{pmatrix} \Phi_4 \\ \Psi_4 \end{pmatrix} + \mathcal{M} \begin{pmatrix} \Phi_4 \\ \Psi_4 \end{pmatrix} \right) d\mathbf{y} = \\ \int \int \int_{R_B} \mathbf{P}_{sc,ss,cc}^T \left(\mathcal{N}_1 \begin{pmatrix} \Phi_\varepsilon \\ \Psi_\varepsilon \end{pmatrix} + \begin{pmatrix} \lambda_2 \Phi_\varepsilon + \lambda_0 \Phi_2 \\ \frac{\tau_0 \lambda_2 + \tau_1 \lambda_1 + \tau_2 \lambda_0}{D} \Psi_\varepsilon + \mu^2 \Psi_2 \end{pmatrix} \right) d\mathbf{y}. \end{aligned} \quad (3.70)$$

Following the steps from (3.33) to (3.43), we arrive at an equation

$$S_\varepsilon \left(2d_1 + \frac{3\mu}{2} \mu_1^2 (h_3 + h_4) \right) = (\tau_2 \lambda_0 + \tau_1 \lambda_1) k_2 + \lambda_0 H_1 - \mu^2 H_2, \quad (3.71)$$

where $\mu^2 = \tau_0 \lambda_0$, $\mu_1^2 = \tau_0 \lambda_1 + \tau_1 \lambda_0$, k_2 is defined in (3.36), h_3 and h_4 are defined in (3.64), and d_1 is given in (3.66). Additionally, $H_1 = \int_0^\infty P_1 \tilde{\Phi}_2(\rho) \rho^2 d\rho$ and $H_2 = \int_0^\infty \tilde{\Psi}_2(\rho) \rho^2 d\rho$, where $\tilde{\Phi}_2$ and $\tilde{\Psi}_2$ are the radial parts of Φ_2 and Ψ_2 , respectively.

We now summarize the solution for the problem in a unit sphere. From (3.45), we calculate the leading order of τ . By solving (3.60), we obtain the first order correction to τ , namely τ_1 , and the leading order of λ_I . By setting λ as purely imaginary in (3.71) and solving it, we obtain τ_2 and λ_1 . Consequently, we compute the HB threshold τ to the $\mathcal{O}(\varepsilon^2)$ correction and the oscillation frequency λ_I to the $\mathcal{O}(\varepsilon)$ correction.

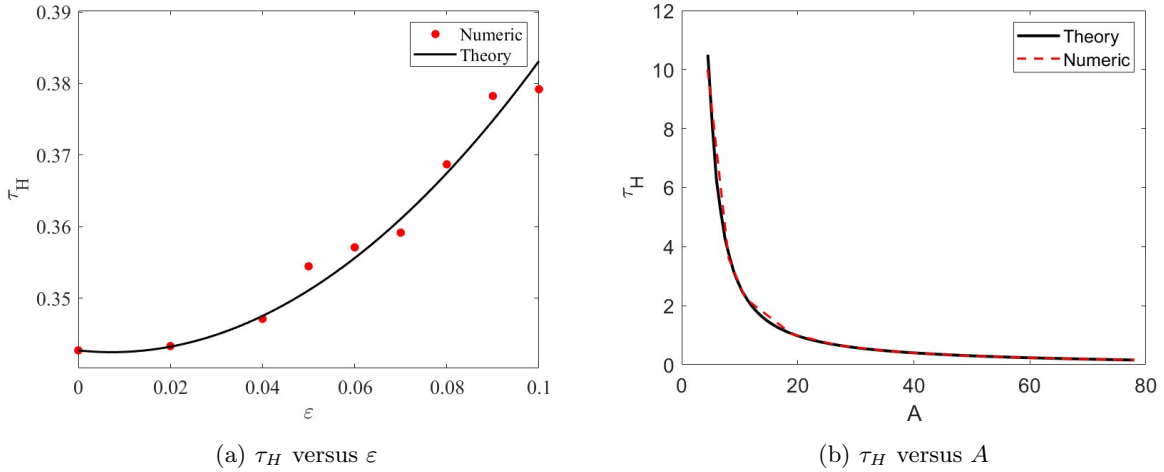


Figure 5: (a) A plot of τ_H , including $\mathcal{O}(\varepsilon^2)$ corrections, versus ε for $S_\varepsilon = 15$. Numerical data are generated using FlexPDE. (b) A plot of τ_H as a function of A with $\varepsilon = 0.03$. Numerical data are generated by solving the full eigenvalue problem in (3.2), and the analytical results show an excellent fit with the numerical data.

In Figure 5a, we use FlexPDE to simulate the problem and generate numerical results for the threshold across various values of ε , ranging from 0 to 0.1, with $S_\varepsilon = 15$. The analytical results show an excellent fit with the numerical data. In Figure 5b, we plot A versus τ_H for $\varepsilon = 0.03$. These comparisons validate the accuracy of the theoretical predictions against computational simulations.

3.2 The perturbed sphere

In this section, we consider the problem on a perturbed sphere with boundary parameterized by $(x_1, x_2, x_3) = (1 + \sigma f(\theta, \varphi))\mathbf{e}$, where $\varepsilon \ll \sigma \ll 1$, $\mathbf{e} = (\sin \theta \cos \varphi, \sin \theta \sin \varphi, \cos \theta)^T$, and $f(\theta, \varphi)$ is a periodic function over the interval $\varphi \in [0, 2\pi)$ and $\theta \in [0, \pi)$. The function $f(\theta, \varphi)$ can be expressed in terms of spherical harmonics as

$$f(\theta, \varphi) = P_n^m(\cos \theta) \cos m\varphi, \quad 0 \leq m \leq n \quad \text{and} \quad n \in \mathbb{N}, \quad (3.72)$$

where $P_n^m(\cos \theta)$ is an associated Legendre polynomial. The negative harmonics result from a rotation of the positive harmonics about the x_3 -axis by $\pi/(2m)$. Thus, we analyze the non-negative harmonics as representatives. In this problem, we aim to gain insight into how the geometry influences the preferred direction of oscillation at onset.

In the following analysis, we show that the $n = 2$ modes affect the bifurcation threshold, oscillatory frequency, and oscillation mode at $\mathcal{O}(\sigma)$. The effect of the perturbation on the domain is to stretch it in one direction, transforming the geometry into an ellipsoid. When $m = 0$, the domain stretches along the x_3 -axis. We focus on the case $n = 2$ and $m = 0$, in which the x_3 -axis is semi-major axis.

We begin by computing the perturbed boundary conditions. The effect of the boundary perturbation on $v(\mathbf{x})$ is minimal due to its localized properties; therefore, we focus on its effect on $u(\mathbf{x})$.

We expand

$$u \sim u_0(\rho) + \sigma u_1(\rho, \theta, \varphi), \quad (3.73)$$

and compute the boundary conditions for u_1 . The outward normal on $\partial\Omega$ is

$$\vec{\mathbf{n}} = (1 + \sigma f)\mathbf{e} - \sigma \frac{f_\varphi \mathbf{e}_\varphi}{\sin^2 \theta} - \sigma f_\theta \mathbf{e}_\theta, \quad (3.74)$$

where f_φ is $\partial_\varphi f(\theta, \varphi)$, f_θ is $\partial_\theta f(\theta, \varphi)$, \mathbf{e}_φ and \mathbf{e}_θ are defined in (3.54).

The boundary condition $\nabla u \cdot \vec{\mathbf{n}} = 0$ becomes

$$u_{0\rho} + \sigma u_{1\rho} - \sigma^2 \frac{f_\varphi u_{1\varphi}}{(1 + \sigma f)^2 \sin^2 \theta} - \sigma^2 \frac{f_\theta u_{1\theta}}{(1 + \sigma f)^2} = 0. \quad (3.75)$$

By collecting the first order of σ in (3.75) and letting $f(\theta, \varphi) = \frac{1}{2}(3 \cos^2 \theta - 1)$, we obtain the boundary conditions

$$u_{0\rho}(1) = 0, \quad u_{1\rho}(1, \theta, \varphi) = -\frac{1}{2}(3 \cos^2 \theta - 1)u_{0\rho\rho}(1). \quad (3.76)$$

We now compute the Hessian term of the Neumann Green's function. We expand $G \sim G_0 + \sigma G_1$, where G_0 is the solution given in (3.59), defined in an unperturbed unit ball with the source at the origin, and G_1 satisfies

$$\Delta G_1 = 0, \quad \mathbf{x} \in \Omega; \quad G_{1\rho}(1, \theta, \varphi) = -\frac{3}{8\pi}(3 \cos^2 \theta - 1). \quad (3.77)$$

Accordingly, the solution is

$$G_1 = -\frac{3}{16\pi}\rho^2(3 \cos^2 \theta - 1). \quad (3.78)$$

Recalling that $x_1 = \rho \sin \theta \cos \varphi$, $x_2 = \rho \sin \theta \sin \varphi$, $x_3 = \rho \cos \theta$, we write $G_1 = \frac{3}{16\pi}(x_1^2 + x_2^2 - 2x_3^2)$ in Cartesian coordinates. Therefore, the Hessian matrix \mathcal{H}_{11} is given by

$$\mathcal{H}_{11} \sim \frac{1}{4\pi}\mathcal{I}_3 + \sigma \frac{3}{8\pi} \begin{pmatrix} 1 & 0 & 0 \\ 0 & 1 & 0 \\ 0 & 0 & -2 \end{pmatrix}. \quad (3.79)$$

For the Helmholtz Green's function G_μ , we expand $G_\mu \sim G_{\mu 0} + \sigma G_{\mu 1}$. Then we compute $\nabla_{\mathbf{x}_1} G_\mu \sim \mathbf{g}_0 + \sigma \mathbf{g}_1$, where \mathbf{g}_0 is given in (3.52), and \mathbf{g}_1 satisfies

$$\begin{aligned} \Delta \mathbf{g}_1 - \mu^2 \mathbf{g} &= 0, \quad \mathbf{x}, \mathbf{x}_0 \in \Omega; \\ \mathbf{g}_{1\rho}(1, \theta, \varphi) &= -f(\theta, \varphi)\mathbf{g}_{0\rho\rho}(1, \theta, \varphi). \end{aligned} \quad (3.80)$$

Therefore, the boundary condition of \mathbf{g}_1 is

$$\mathbf{g}_{1\rho} = \begin{pmatrix} \mathbf{g}_{1\rho}^{(1)} \\ \mathbf{g}_{1\rho}^{(2)} \\ \mathbf{g}_{1\rho}^{(3)} \end{pmatrix} = \frac{1}{2}(3 \cos^2 \theta - 1)F''(1) \begin{pmatrix} \sin \theta \cos \varphi \\ \sin \theta \sin \varphi \\ \cos \theta \end{pmatrix}. \quad (3.81)$$

Further, we use normalized real Spherical Harmonics Y_n^m to express the boundary conditions, which is

$$\mathbf{g}_{1\rho}^{(k)} = \frac{3}{4}(c_{1k}Y_3^m + c_{2k}Y_1^m) \left(\frac{\mu}{2\pi}\right)^{\frac{3}{2}} F''(1), \quad k = 1, 2, 3, \quad m = -1, 0, 1, \quad (3.82)$$

where

$$\begin{aligned} Y_n^1 &= -\sqrt{2}\sqrt{\frac{2n+1}{4\pi n(n+1)}}P_n^1(\cos \theta) \cos \varphi, \quad Y_n^0 = \sqrt{\frac{2n+1}{4\pi}}P_n^0(\cos \theta), \\ Y_n^{-1} &= -\sqrt{2}\sqrt{\frac{2n+1}{4\pi n(n+1)}}P_n^1(\cos \theta) \sin \varphi, \quad n = 1, 3, \\ c_{11} = c_{12} &= \frac{12}{5}\sqrt{\frac{2\pi}{21}}, \quad c_{21} = c_{22} = -6\sqrt{\frac{\pi}{3}}, \quad c_{13} = \frac{12}{5}\sqrt{\frac{\pi}{7}}, \quad c_{33} = -\frac{12}{5}\sqrt{\frac{\pi}{3}}. \end{aligned} \quad (3.83)$$

We then solve \mathbf{g}_1 in (3.80) with boundary conditions given in (3.83) and get

$$\begin{aligned}\mathbf{g}_1^{(1)} &= A_1(\rho)Y_3^1 + B_1(\rho)Y_1^1, \\ \mathbf{g}_1^{(2)} &= A_1(\rho)Y_3^{-1} + B_1(\rho)Y_1^{-1}, \\ \mathbf{g}_1^{(3)} &= A_2(\rho)Y_3^0 + B_2(\rho)Y_3^0,\end{aligned}\tag{3.84}$$

where

$$\begin{aligned}A_1(\rho) &= \frac{12\sqrt{\frac{2\pi}{21}}\left(\frac{\mu}{2\pi}\right)^{\frac{3}{2}}F''(1)I_{7/2}(\mu\rho)\rho^{-\frac{1}{2}}}{5(\mu I'_{7/2}(\mu) - \frac{1}{2}I_{7/2}(\mu))}, & B_1(\rho) &= -\frac{6\sqrt{\frac{\pi}{3}}\left(\frac{\mu}{2\pi}\right)^{\frac{3}{2}}F''I_{3/2}(\mu\rho)\rho^{-\frac{1}{2}}}{(\mu I'_{3/2}(\mu) - \frac{1}{2}I_{3/2}(\mu))}, \\ A_2(\rho) &= \frac{12\sqrt{\frac{\pi}{7}}\left(\frac{\mu}{2\pi}\right)^{\frac{3}{2}}F''(1)I_{7/2}(\mu\rho)\rho^{-\frac{1}{2}}}{5(\mu I'_{7/2}(\mu) - \frac{1}{2}I_{7/2}(\mu))}, & B_2(\rho) &= -\frac{12\sqrt{\frac{\pi}{3}}\left(\frac{\mu}{2\pi}\right)^{\frac{3}{2}}F''(1)I_{3/2}(\mu\rho)\rho^{-\frac{1}{2}}}{5(\mu I'_{3/2}(\mu) - \frac{1}{2}I_{3/2}(\mu))}.\end{aligned}\tag{3.85}$$

Now we take gradient on \mathbf{g}_1 respect to \mathbf{x} using $\nabla_{\mathbf{x}} = \partial_\rho \mathbf{e} + \rho^{-1} \sin^{-2} \theta \partial_\varphi \mathbf{e}_\varphi + \rho^{-1} \partial_\theta \mathbf{e}_\theta$ to obtain

$$\begin{aligned}\nabla_{\mathbf{x}} \mathbf{g}_1^{(1)} &= (A'_1(\rho)Y_3^1 - B'_1(\rho)Y_1^1) \mathbf{e} + \frac{1}{\rho \sin^2 \theta} (A_1(\rho) \partial_\varphi Y_3^1 - B_1(\rho) \partial_\varphi Y_1^1) \mathbf{e}_\varphi \\ &\quad + \frac{1}{\rho} (A_1(\rho) \partial_\theta Y_3^1 - B_1(\rho) \partial_\theta Y_1^1) \mathbf{e}_\theta,\end{aligned}\tag{3.86}$$

where

$$\begin{aligned}A'_1(\rho) &= \frac{12\sqrt{\frac{2\pi}{21}}\left(\frac{\mu}{2\pi}\right)^{\frac{3}{2}}F''(1)}{5(\mu I'_{7/2}(\mu) - \frac{1}{2}I_{7/2}(\mu))} \left(\mu I'_{7/2}(\mu\rho)\rho^{-\frac{1}{2}} - \frac{1}{2}I_{7/2}(\mu\rho)\rho^{-\frac{3}{2}} \right), \\ B'_1(\rho) &= -\frac{6\sqrt{\frac{\pi}{3}}\left(\frac{\mu}{2\pi}\right)^{\frac{3}{2}}F''}{(\mu I'_{3/2}(\mu) - \frac{1}{2}I_{3/2}(\mu))} \left(\mu I'_{3/2}(\mu\rho)\rho^{-\frac{1}{2}} - \frac{1}{2}I_{3/2}(\mu\rho)\rho^{-\frac{3}{2}} \right).\end{aligned}\tag{3.87}$$

By setting $\rho = \rho_0 \rightarrow 0^+$ and using the properties of the Bessel function of the second kind for small arguments, we obtain

$$\nabla_{\mathbf{x}} \mathbf{g}_1^{(1)} = -\frac{F''(1)\mu^3}{2\pi^2(\mu I'_{3/2}(\mu) - \frac{1}{2}I_{3/2}(\mu))} \begin{pmatrix} 1 \\ 0 \\ 0 \end{pmatrix}\tag{3.88}$$

Following the same process, we can compute $\nabla_{\mathbf{x}} \mathbf{g}_1^{(2)}$ and $\nabla_{\mathbf{x}} \mathbf{g}_1^{(3)}$, and then we end up with

$$\nabla_{\mathbf{x}} \mathbf{g}_1 = -\frac{F''(1)\mu^3}{\pi^2(\mu I'_{3/2}(\mu) - \frac{1}{2}I_{3/2}(\mu))} \begin{pmatrix} \frac{1}{2} & 0 & 0 \\ 0 & \frac{1}{2} & 0 \\ 0 & 0 & \frac{1}{5} \end{pmatrix}.\tag{3.89}$$

Note that the leading order of $\mathcal{Q}\mu_1$ is the same as in an unperturbed unit ball. Therefore, \mathcal{Q}_{μ_1} in the perturbed ball is given by

$$\mathcal{Q}_{\mu_1} = -\frac{(\pi + 2Q(\mu))\mu^3}{12\pi^2} \mathcal{I}_3 - \sigma \frac{F''(1)\mu^3}{\pi^2(\mu I'_{3/2}(\mu) - \frac{1}{2}I_{3/2}(\mu))} \begin{pmatrix} \frac{1}{2} & 0 & 0 \\ 0 & \frac{1}{2} & 0 \\ 0 & 0 & \frac{1}{5} \end{pmatrix}.\tag{3.90}$$

We now substitute (3.79) and (3.90) into (3.48) yielding a system containing τ and λ . We perturb $\lambda_0 = (\lambda_{00} + \sigma\lambda_{01})i$, $\lambda_1 = (\lambda_{10} + \sigma\lambda_{11})i$, $\tau_0 = \tau_{00} + \sigma\tau_{01}$ and $\tau_1 = \tau_{10} + \sigma\tau_{11}$. From (3.45) and given that λ_{00} is not zero, the value of τ_{00} and τ_{01} are

$$\tau_{00} = \frac{k_1}{k_2}, \quad \tau_{01} = 0,\tag{3.91}$$

where k_1 and k_2 are defined in (3.36). Since λ_0 is purely imaginary, we write $\mu^2 = \tau_0\lambda_0 = \mu_0^2 i + \sigma\mu_1^2 i$, where $\mu_0^2 = \tau_{00}\lambda_{00}$ and $\mu_1^2 = \tau_{00}\lambda_{01}$. Next we substitute (3.79) and (3.90) into (3.48) and collect the leading order as well

as $\mathcal{O}(\sigma)$ terms, respectively, to obtain

$$12\pi S_\varepsilon \left(-\frac{(\pi + 2Q(\mu))\mu^3}{12\pi^2} - \frac{D}{4\pi} \right) \begin{pmatrix} a_1 \\ a_2 \\ a_3 \end{pmatrix} = k_2 \tau_{10} \lambda_{00} i \begin{pmatrix} a_1 \\ a_2 \\ a_3 \end{pmatrix}, \quad (3.92a)$$

$$12\pi S_\varepsilon (Q_{\mu\sigma} - D\mathcal{H}_\sigma) \begin{pmatrix} a_1 \\ a_2 \\ a_3 \end{pmatrix} = k_2 (\tau_{10} \lambda_{01} + \tau_{11} \lambda_{00}) i \begin{pmatrix} a_1 \\ a_2 \\ a_3 \end{pmatrix}, \quad (3.92b)$$

where

$$Q_{\mu\sigma} = -\frac{F''(1)\mu_1^3}{\pi^2(\mu_1 I_{3/2}(\mu_1) - \frac{1}{2}I_{3/2}(\mu_1))} \begin{pmatrix} \frac{1}{2} & 0 & 0 \\ 0 & \frac{1}{2} & 0 \\ 0 & 0 & \frac{1}{5} \end{pmatrix}, \quad \mathcal{H}_\sigma = \frac{3}{8\pi} \begin{pmatrix} 1 & 0 & 0 \\ 0 & 1 & 0 \\ 0 & 0 & -2 \end{pmatrix}.$$

From (3.91) and (3.92a), we find that the leading order and the $\mathcal{O}(\varepsilon)$ terms of the threshold are the same for all three directions, while the $\mathcal{O}(\varepsilon\sigma)$ terms of τ differ. Thus, we conclude that the preferred mode of oscillation is determined by the value of τ_{11} solved in (3.92b). In this geometry, we numerically observe that the value of τ_{11} corresponding to the $(0, 0, 1)$ -direction is smaller than in the other two directions. Therefore, the threshold for the $(0, 0, 1)$ -direction is reached first as τ increases, indicating that the dominant mode of translational oscillation is along the major axis. Furthermore, the threshold in the perturbed domain is smaller than that in the unperturbed sphere due to the negative value of τ_{11} in the perturbed sphere.

We now briefly discuss the effect of perturbations of the form $f(\theta, \varphi)$ when $n \neq 2$. For $n = 0$, the domain is a sphere with radius $(1 + \sigma)$ since $f(\theta, \varphi) = 1$. For $n = 1$, $m = 0$ or $m = 1$, the perturbation constitutes a translation of the unit ball by σ along one axis. For example, the equation for the perturbed sphere, when $m = 0$ and $f(\theta, \varphi) = \cos \theta$, is

$$x_1^2 + x_2^2 + (x_3 - \sigma)^2 = [1 + \frac{\sigma^2}{8}(3 - \cos 2\varphi + 2 \cos^2 \varphi \cos 2\theta)]^2. \quad (3.93)$$

This perturbation is equivalent to translating the sphere in the x_3 -direction, accompanied by a $\mathcal{O}(\sigma^2)$ dilation of the sphere's shape. For $n \geq 3$, the leading order correction to the Neumann Green's function is an $\mathcal{O}(\rho^n)$ function, which has no impact on the Hessian. For the gradient of the Helmholtz Green's function with respect to the source location, $\nabla_{\mathbf{x}_1} G_\mu(\mathbf{x}; \mathbf{x}_1)$, the first order correction is a function of $(I_{n-\frac{1}{2}}(z)z^{-\frac{1}{2}} + I_{n+\frac{3}{2}}(z)z^{-\frac{1}{2}}) \sim \mathcal{O}(z^{n-1})$ and they are not affecting the value of $\mathcal{Q}_{\mu 1}$ in the eigenvalue problem.

3.3 The defected sphere

We now discuss the translational oscillatory instability of one spot pattern on a defected domain. In [24], a technique for converting the defect to a localized pinned spot is introduced for a 2D problem. We apply the same technique and extend it to a 3D domain. We firstly define the defected domain. In this geometry, we remove a ball-shaped defect with a radius of $\mathcal{O}(\varepsilon)$ from the domain, from which the chemicals are leaking. The defect is modeled by

$$\Omega_\varepsilon = \{\mathbf{x} \in \Omega : |\mathbf{x} - \mathbf{x}_0| \leq \varepsilon C\}, \quad (3.94)$$

where $C > 0$ is an $\mathcal{O}(1)$ constant that controls the size of the defect. The equilibrium construction of this problem is provided in Appendix A.

In this analysis, we treat the defect as a pinned spot, hence we can extend the result in Section 3. In the inner region near the defect, it is readily to see that $\Psi_{\varepsilon 0}$ is zero, and the leading order to Ψ_0 is $\mathcal{O}(\varepsilon^2)$. Therefore, we have

$$\Delta_{\mathbf{y}} \Psi_{20} - (2U_{\varepsilon 0} V_{\varepsilon 0} \Phi_{20} + V_{\varepsilon 0}^2 \Psi_{20}) = 0; \quad \Psi_{20} = 0 \quad \text{on} \quad |\mathbf{y}| = C. \quad (3.95)$$

The solution of Ψ_{20} is given by

$$\Psi_{20} = \kappa_0 \partial_{s_{\varepsilon 0}} U_{\varepsilon 0}, \quad (3.96)$$

thus the far-filed behavior is

$$\Psi_{20} \sim \kappa_0 \left(\frac{1}{C} - \frac{1}{\rho_0} \right), \quad (3.97)$$

where $U_{\varepsilon 0}$ is computed in (A.6). Here κ_0 is a constant determined by matching with the outer solution.

The behavior of the spot in the inner region is similar to that of the one spot problem on a general domain. We change the notation of (3.6) and (3.13), yielding

$$\begin{aligned}\Psi_{\varepsilon 1} &= \mathbf{a}_1^T \mathbf{e}_1 \partial_{\rho_1} U_{\varepsilon 1}, \quad \Psi_{\varepsilon 1} \sim \mathbf{a}_1^T \mathbf{e}_1 \frac{S_{\varepsilon 1}}{\rho_1^2} \quad \text{as } \rho_1 \rightarrow \infty; \\ \Psi_{21} &\sim \kappa_1 \left(\chi'(S_{\varepsilon 1}) - \frac{1}{\rho_1} \right) - \mathbf{a}_1^T \mathbf{e}_1 S_{\varepsilon 1} \frac{\tau_0 \lambda_0}{2} \quad \text{as } \rho_1 \rightarrow \infty.\end{aligned}\tag{3.98}$$

In the outer region, we use the same notation from Section 3 and have

$$\begin{aligned}\Delta \psi_\varepsilon - \mu_\varepsilon^2 \psi_\varepsilon &= 0, \quad x \in \Omega; \\ \psi_\varepsilon &\sim \kappa_0 \left(\frac{1}{C} - \frac{\varepsilon}{|\mathbf{x} - \mathbf{x}_0|} \right), \quad \text{as } \mathbf{x} \rightarrow \mathbf{x}_0; \\ \psi_\varepsilon &\sim \frac{S_{\varepsilon 1} \mathbf{a}^T (\mathbf{x} - \mathbf{x}_1)}{|\mathbf{x} - \mathbf{x}_1|^3} + \kappa_1 \left(\chi'(S_{\varepsilon 1}) - \frac{\varepsilon}{|\mathbf{x} - \mathbf{x}_1|} \right) - \frac{\mathbf{a}^T \mathbf{e}_1 S_{\varepsilon 1} \mu^2}{2}, \quad \text{as } \mathbf{x} \rightarrow \mathbf{x}_1,\end{aligned}\tag{3.99}$$

Hence the new ψ_ε is

$$\begin{aligned}\psi_\varepsilon &= -4\pi \left[S_{\varepsilon 1} \mathbf{a}^T \nabla_{\mathbf{x}_1} G_\mu(\mathbf{x}; \mathbf{x}_1) - \varepsilon \kappa_1 G_\mu(\mathbf{x}; \mathbf{x}_1) \right. \\ &\quad \left. + \varepsilon (\tau_0 \lambda_1 + \tau_1 \lambda_0) S_{\varepsilon 1} \mathbf{a}^T \partial_{\mu^2} \nabla_{\mathbf{x}_1} G_\mu(\mathbf{x}; \mathbf{x}_1) - \kappa_0 \varepsilon G_\mu(\mathbf{x}; \mathbf{x}_0) \right],\end{aligned}\tag{3.100}$$

which includes one additional term compared to (3.21). The local behavior of $\nabla_{\mathbf{x}_1} G_\mu(\mathbf{x}; \mathbf{x}_1)$ near the spot location is given in (3.16) and (2.8). While near the defect, the local behavior of $\nabla_{\mathbf{x}_1} G_\mu(\mathbf{x}; \mathbf{x}_1)$ is

$$\nabla_{\mathbf{x}_1} G_\mu(\mathbf{x}; \mathbf{x}_1) \sim \nabla_{\mathbf{x}_1} G_\mu(\mathbf{x}_0; \mathbf{x}_1), \quad \text{as } \mathbf{x} \rightarrow \mathbf{x}_0.\tag{3.101}$$

Matching (3.100) with (3.99) and using (3.16) and (3.101), we obtain the constants κ_0 and κ_1 ,

$$\begin{aligned}\kappa_0 &= -4\pi C S_{\varepsilon 1} \mathbf{a}^T \nabla_{\mathbf{x}_1} G_\mu(\mathbf{x}_0; \mathbf{x}_1); \\ \kappa_1 &= -\frac{4\pi S_{\varepsilon 1}}{\chi'(S_{\varepsilon 1})} \mathbf{a}^T \nabla_{\mathbf{x}} R_\mu(\mathbf{x}; \mathbf{x}_1)|_{\mathbf{x}=\mathbf{x}_1}.\end{aligned}\tag{3.102}$$

In particular, the presence of the defect breaks the symmetric of the geometry. Therefore, the value of $\nabla_{\mathbf{x}} R_\mu(\mathbf{x}; \mathbf{x}_1)|_{\mathbf{x}=\mathbf{x}_1}$, which is zero in a unit sphere, is non-zero here.

We next apply solvability conditions on the system of $\mathcal{O}(\varepsilon^2)$ and $\mathcal{O}(\varepsilon^3)$ in the inner region. By expanding (3.100), we obtain the far-field behavior of \mathbf{W}_1 , as $\rho_1 \rightarrow \infty$,

$$\mathbf{W}_1 \sim \begin{pmatrix} 0 \\ -4\pi \left[S_{\varepsilon 1} \mathbf{a}^T \left(\varepsilon \mathcal{Q}_{\mu 1} \rho_1 + \frac{\mu_\varepsilon^2}{8\pi} \right) \mathbf{e}_1 - \kappa_1 \left(\chi'(S_{\varepsilon 1}) - \frac{1}{\rho_1} \right) - \varepsilon \kappa_1 R_\mu(\mathbf{x}_1; \mathbf{x}_1) - \varepsilon \kappa_0 G_\mu(\mathbf{x}_1; \mathbf{x}_0) \right] \end{pmatrix}.\tag{3.103}$$

We then multiply (3.23) by $\mathbf{P}_{sc,ss,cc}$, which is defined in (3.29), on both side of (3.23) and then integrate over a ball with radius $R \gg 1$ centered at the origin. Hence we have

$$\begin{aligned}& \int \int \int_{B_R} \mathbf{P}_{sc,ss,cc}^T [\Delta_{\mathbf{y}} \mathbf{W}_1 + \mathcal{M}_1 \mathbf{W}_1] d\mathbf{y} \\ &= \int \int \int_{B_R} \mathbf{P}_{sc,ss,cc}^T \left[\begin{pmatrix} (\lambda_0 + \varepsilon \lambda_1) \Phi_{\varepsilon 1} \\ \frac{\mu_\varepsilon^2}{D} \Psi_{\varepsilon 1} \end{pmatrix} + \mathcal{N}_1 \begin{pmatrix} \Phi_{\varepsilon 1} \\ \Psi_{\varepsilon 1} \end{pmatrix} \right] d\mathbf{y}.\end{aligned}\tag{3.104}$$

Following the process from (3.33) to (3.43) in Section 3, but using the far-field condition of W_1 given in (3.103), we derive an eigenvalue system,

$$\frac{12\pi}{\tau_1 k_2} [S_{\varepsilon 1} (\mathcal{Q}_{\mu 1} - \mathcal{H}_{11})^T - S_{\varepsilon 0} \mathcal{H}_{10}^T] \mathbf{a} = \lambda_0 \mathbf{a},\tag{3.105}$$

where $\mathcal{Q}_{\mu 1}$ is defined in (3.18), and \mathcal{H}_{11} , \mathcal{H}_{10} are given in (1.3). Note that $\mathcal{Q}_{\mu 1}$ here differs from that in a sphere or a perturbed sphere where the spot is located at the domain center. A general form of the regular part of the Helmholtz Green's function is provided in Appendix B.

From (3.45) and (3.105), we observe that the HB threshold is closely related to the source strength $S_{\varepsilon 1}$. However, for a fixed feed rate A , the defect competes with the spot for resources according to (A.12). Furthermore, as the defect size, measured by C , increases, more chemicals leak out, resulting in a smaller $S_{\varepsilon 1}$ at equilibrium. The value of the HB threshold increases with increasing C (see Figure 6), indicating that for a large C , the HB threshold is more difficult to reach. Therefore, for a fixed feed rate A , the translational oscillatory instability is more difficult to trigger in the defected domain than in a normal domain (without a defect). Moreover, when $S_{\varepsilon 1}$ falls below a certain critical value, an amplitude oscillatory instability occurs. Further details are provided in Section 4.

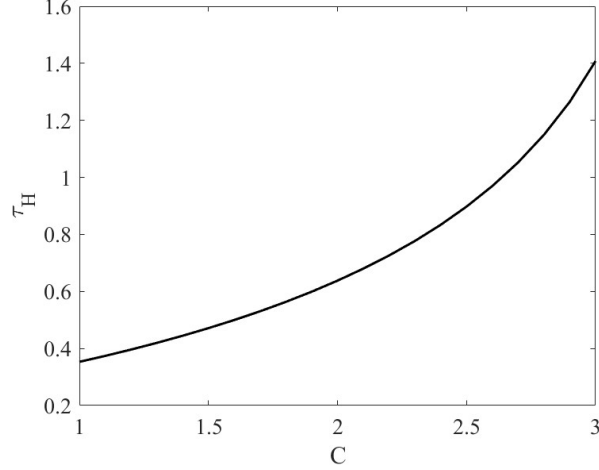


Figure 6: Plot of the translational instability threshold τ_H versus C in the defected domain, where the defect is a small disk radius εC .

4 The stability analysis: Large eigenvalues

In this section, we discuss the amplitude instability of the spot on a general domain. We assume $\lambda \sim \mathcal{O}(1)$ and investigate how the Bifurcation threshold τ changes with the feed rate A in the system. When A is less than 13.56, the scaling of τ is $\mathcal{O}(1)$. As A increases, the scaling of τ becomes $\mathcal{O}(\varepsilon^{-3})$. Lastly, we compare the result with the translational oscillatory instability threshold and obtaining the intercept of the HB threshold, at which the dominant instability changes.

4.1 The $\tau \sim \mathcal{O}(1)$ regime

In this subsection, we compute the $\mathcal{O}(1)$ HB threshold. The eigenvalue problem is given in (3.2). In the inner region, we expand

$$\phi = P_n^m(\cos \theta) e^{im\varphi} (\Phi_\varepsilon(\rho) + \dots), \quad \psi = P_n^m(\cos \theta) e^{im\varphi} (\Psi_\varepsilon(\rho) + \dots). \quad (4.1)$$

Substituting (4.1) into (3.2), we derive the radially symmetric eigenvalue problem

$$\begin{aligned} \lambda \Phi_\varepsilon &= \Delta_n \Phi_\varepsilon - \Phi_\varepsilon + 2U_\varepsilon V_\varepsilon \Phi_\varepsilon + V_\varepsilon^2 \Psi_\varepsilon, \\ 0 &= \Delta_n \Psi_\varepsilon - (2U_\varepsilon V_\varepsilon \Phi_\varepsilon + V_\varepsilon^2 \Psi_\varepsilon), \end{aligned} \quad (4.2)$$

where $\Delta_n = \partial_{\rho\rho} + 2\rho^{-1}\partial_\rho - n(n+1)\rho^{-2}$.

We now consider $n = 0$ which corresponding to the instability of the spot's amplitude. Since V_ε decays exponentially as ρ tends to infinity, by rescaling the eigenfunction, we get the far-field of Ψ_ε as

$$\Psi_\varepsilon \sim B(\lambda, S_\varepsilon) - \frac{1}{\rho}, \quad \rho \rightarrow \infty. \quad (4.3)$$

Using the divergence theorem on the second equation of (4.2), we have

$$\int_{\Omega} 2U_\varepsilon V_\varepsilon \Phi_\varepsilon + V_\varepsilon^2 \Psi_\varepsilon d\mathbf{y} = 4\pi. \quad (4.4)$$

Using (4.4), we have

$$\int_{\Omega} \frac{1}{\varepsilon^3} (2u_e v_e \phi + v_e^2 \psi) d\mathbf{x} \sim 4\pi, \quad (4.5)$$

and the outer problem is

$$\Delta\psi - \frac{\tau\lambda\varepsilon}{D}\psi = \frac{4\pi\varepsilon}{D}\delta(\mathbf{x}). \quad (4.6)$$

The solution to (4.6) is

$$\psi = -\frac{\varepsilon}{\sqrt{D}r(1+\bar{Q}(\mu))} (e^{\mu r} + \bar{Q}(\mu)e^{-\mu r}), \quad r = |\mathbf{x}|, \quad \bar{Q}(\mu) = \frac{e^{2\mu}(\mu-1)}{\mu+1}, \quad \mu = \sqrt{\frac{\tau\lambda\varepsilon}{D}}. \quad (4.7)$$

Expanding ψ for small r and matching with (4.3), we obtain

$$B(\lambda, S_\varepsilon) = -\frac{\varepsilon\mu(1-\bar{Q}(\mu))}{\sqrt{D}(1+\bar{Q}(\mu))}. \quad (4.8)$$

Assume that $\mu \ll 1$, the equation (4.8) can be simplified as

$$B(\lambda, S_\varepsilon) = -\frac{3\varepsilon}{\mu^2\sqrt{D}} + \frac{9\varepsilon}{5\sqrt{D}} + \mathcal{O}(\mu^2). \quad (4.9)$$

By substituting $\mu = \sqrt{\varepsilon\tau\lambda}$ into (4.9) and collecting the leading order, we obtain

$$B(\lambda, S_\varepsilon) = -\frac{3\sqrt{D}}{\tau\lambda}. \quad (4.10)$$

To seek the possibility of the instability arises by Hopf bifurcation, we let $\lambda = \lambda_I i$, and separate (4.10) into real and imaginary parts, yielding

$$\mathbf{Re}(B(\lambda_I, S_\varepsilon)) = 0, \quad (4.11a)$$

$$\mathbf{Im}(B(\lambda_I, S_\varepsilon)) = \frac{3\sqrt{D}}{\tau\lambda_I}. \quad (4.11b)$$

We now numerically compute the value of $B(\lambda_I, S_\varepsilon)$ by solving (4.2) with the far-field behavior in (4.3).

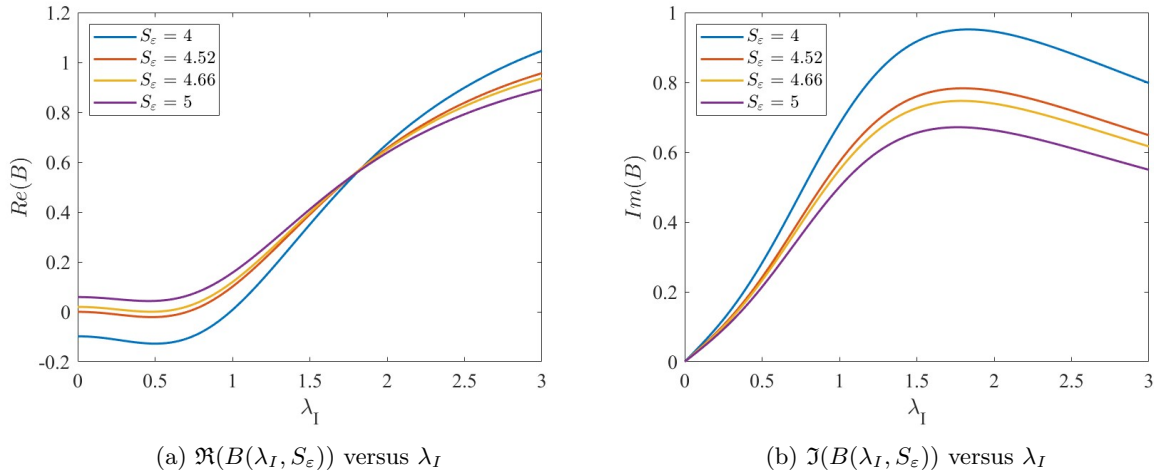


Figure 7: (a) Real part of $B(\lambda_I, S_\varepsilon)$ and (b) imaginary part of $B(\lambda_I, S_\varepsilon)$ for $S_\varepsilon = 4, 4.52, 4.66$ and 5 . Here λ_I is the pure imaginary eigenvalue.

In Figure 7a, the value of $\Re(B)$ increases as S_ε increases when $\lambda_I < 1.5$. When $S_\varepsilon < 4.52$, the curve crosses the $\Re(B) = 0$ once, indicating a single solution for (4.11a). When $S_\varepsilon = 4.52$, we observe that $\lambda_I = 0$ is one of the

solutions according to (4.11a). To verify this, we set $\lambda_I = 0$ in (4.2) and find that the corresponding solution is obtained by differentiating the solution to the core problem with respect to S_ε . Thus, we have $\Re(B(0, S_\varepsilon)) = \chi'(S_\varepsilon)$. Given the required condition $\Re(B) = 0$, we conclude that the critical value of S_ε is 4.52 where $\chi'(S_\varepsilon) = 0$ from Figure 2. For $4.52 \leq S_\varepsilon < 4.66$, two solutions can be found for (4.11a), indicating that two distinct thresholds exist of τ in this range of S_ε . As S_ε increases beyond 4.66, the curve no longer touches the line $\Re(B) = 0$, so there is no solution when $S_\varepsilon > 4.66$.

By using the Taylor expansion on $B(\lambda_I, S_\varepsilon)$ around the point $(\lambda_I, S_\varepsilon) = (0, 4.52)$, we have

$$\lambda_{IH} \sim \frac{|\Re(B_\lambda)| - \alpha}{\Re(B_{\lambda\lambda})}, \quad \tau_H \sim \frac{3\Re(B_{\lambda\lambda})^2}{\beta_2(S_\varepsilon - 4.52) - \alpha\beta_1}, \quad \text{as } S_\varepsilon \rightarrow 4.52^+, \quad (4.12)$$

where B_λ is $\partial_{\lambda_I} B(\lambda_I, S_\varepsilon)$, $B_{\lambda\lambda} = \partial_{\lambda_I \lambda_I} B(\lambda_I, S_\varepsilon)$ and $\alpha = \sqrt{\Re(B_\lambda)^2 - 2\Re(B_{\lambda\lambda})\Re(B_s)(S_\varepsilon - 4.52)}$ with $B_s = \partial_{S_\varepsilon} B(\lambda_I, S_\varepsilon)$, $\beta_1 = 2\Re(B_\lambda)\Im(B_\lambda) - \Im(B)$ and $\beta_2 = 2\Re(B_s)\Im(B_\lambda)\Re(B_{\lambda\lambda})^2$. Note that $B(\lambda_I, S_\varepsilon) = B(-\lambda_I, S_\varepsilon)$, hence $\Re(B_\lambda)$ tends to zero when $\lambda_I \rightarrow 0^+$, which implies λ_{IH} to approach zero and τ_H to diverge.

We now solve the transcendental equations in (4.11) to obtain the values of the amplitude oscillatory frequency and the oscillatory threshold. The resulting bifurcation threshold τ_H and the corresponding eigenvalues λ_{IH} are shown in Figure 8. It shows that there is a unique HB threshold for $S_\varepsilon < 4.52$ and two thresholds when S_ε is between

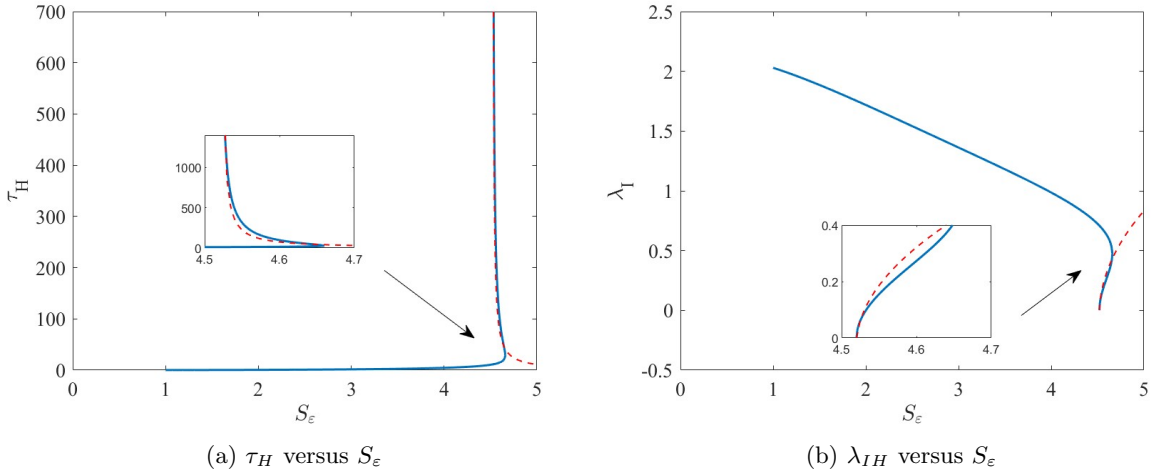


Figure 8: (a) The HB threshold τ_H and (b) eigenvalues λ_{IH} are plotted versus S_ε in the $\tau \sim \mathcal{O}(1)$ regime. In (a), τ_H diverges as $S_\varepsilon \rightarrow 4.52^+$. Two thresholds exist within the range $4.52 < S_\varepsilon < 4.66$, while no thresholds are found for $S_\varepsilon > 4.66$. In (b), the corresponding eigenvalue approaches zero as $S_\varepsilon \rightarrow 4.52^+$. The red dashed line in both plots represents the asymptotic results for τ_H and λ_{IH} , respectively, as given in (4.12).

4.52 and 4.66. The limiting asymptotic behavior given in (4.12) agrees well with the numerical results from (4.11) as $S_\varepsilon \rightarrow 4.52^+$. There is no HB threshold for $S_\varepsilon > 4.66$ in this regime.

In Figure 8, two distinct critical values of τ can be found when $4.52 \leq S_\varepsilon < 4.66$. To investigate how a pair of conjugate eigenvalues cross the imaginary axis, we track the behavior of the eigenvalues by setting $S_\varepsilon = 4.6$. Starting with a small τ (below the smaller HB threshold), we gradually increase τ until it surpasses the larger HB threshold. In Figure 9, the eigenvalues cross from the left half-plane to the right half-plane when τ exceeds the smaller τ_H , making the system unstable to amplitude oscillations. Later they return to the left half-plane as τ continues to increase beyond the larger HB threshold, and the system becomes stable again. As τ increases further, two complex eigenvalues collide and combine at zero-imaginary axis, becoming real and negative. As a result, the system transitions through stable-unstable-stable phases with respect to amplitude oscillatory instability as τ increases.

From Figure 8, no Hopf bifurcation occurs when $S_\varepsilon > 4.66$. We denote this point as a saddle node. Next, we examine how the saddle-node varies with changes in ε . From (4.11), the saddle-node values are identified as $(\lambda_I^0, S_\varepsilon^0, \tau_H^0) = (0.4848, 4.66, 27.66)$. We then perturb

$$\lambda_I^s \sim \lambda_I^0 + \varepsilon^{\delta_1} \lambda_I^1, \quad S_\varepsilon^s \sim S_\varepsilon^0 + \varepsilon^{\delta_2} S_\varepsilon^1, \quad \tau_H^s \sim \tau_H^0 + \varepsilon^{\delta_3} \tau_H^1, \quad (4.13)$$

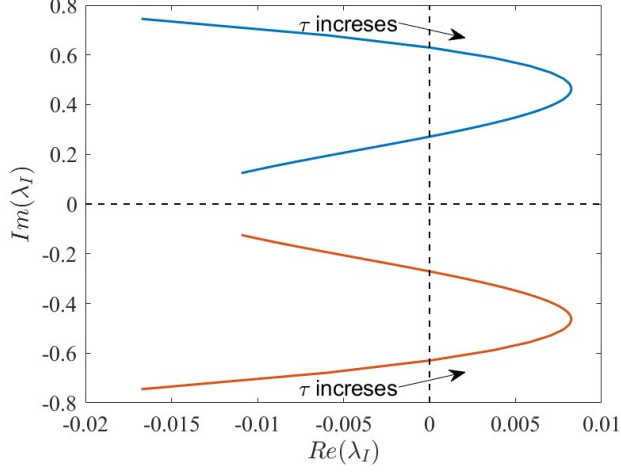


Figure 9: Trajectory of a pair of complex eigenvalues for $S_\varepsilon = 4.6$ as τ increases. As τ increases, the eigenvalues cross from the left half-plane (LHP) to the right half-plane (RHP) when τ exceeds the smaller τ_H . They later return to the LHP as τ continues to increase beyond the larger τ_H .

where $\lambda_I^s, S_\varepsilon^s, \tau_H^s$ are the values at the saddle-node for $\varepsilon > 0$. To compute the values of $\delta_{1,2,3}$, we apply Taylor expansion on $B(\lambda_I, S_\varepsilon)$ around the point $(\lambda_I^0, S_\varepsilon^0, \tau_H^0)$ and substitute to (4.9), yielding

$$B(\lambda_I^0, S_\varepsilon^0) + \varepsilon^{\delta_2} S_\varepsilon^1 B_s(\lambda_I^0, S_\varepsilon^0) + \varepsilon^{\delta_1} \lambda_I^1 B_\lambda(\lambda_I^0, S_\varepsilon^0) + \varepsilon^{\delta_1 + \delta_2} \lambda_I^1 S_\varepsilon^1 B_{\lambda s}(\lambda_I^0, S_\varepsilon^0) = \frac{3i}{(\tau_H^0 + \varepsilon^{\delta_3} \tau_H^1)(\lambda_I^0 + \varepsilon^{\delta_1} \lambda_I^1)} + \frac{9\varepsilon}{5}. \quad (4.14)$$

Thus we obtain $\delta_1 = \delta_2 = \frac{1}{2}$ and $\delta_3 = 1$. To compute $(\lambda_I^1, S_\varepsilon^1, \tau_H^1)$, in addition to solving the real and imaginary parts of (4.14), one additional condition is required. Since the saddle-node is defined as the fold point of B at which the real part of $B(\lambda_I^s, S_\varepsilon^s)$ is tangent to the horizontal line $y = \frac{9\varepsilon}{5}$, we determine the additional condition as follows:

$$\Re(B_\lambda(\lambda_I^s, S_\varepsilon^s)) = 0. \quad (4.15)$$

By solving (4.14) and (4.15) and incorporating (4.13), we derive $\lambda_I^s, S_\varepsilon^s$ and τ_H^s as a function of ε , respectively.

| ε | Theoretical results | | | | Numerical results | | |
|-------------------|---------------------|--------|--------|--------|-------------------|--------|--------|
| | 0 | 0.025 | 0.03 | 0.04 | 0.025 | 0.03 | 0.04 |
| λ_I^s | 0.485 | 0.458 | 0.453 | 0.443 | 0.456 | 0.453 | 0.444 |
| S_ε^s | 4.660 | 5.027 | 5.124 | 5.376 | 5.006 | 5.091 | 5.277 |
| τ_H^s | 27.660 | 34.467 | 35.887 | 39.540 | 34.468 | 35.888 | 39.550 |

Table 1: Theoretical values and numerical values of the saddle nodes for various ε . The theoretical values are computed by solving (4.14) and (4.15). The numerical values are derived from the full eigenvalue problem in regime 1, where there is only one value of λ_I corresponds to S_ε .

Table 1 compares the theoretical and numerical results. The numerical results are obtained by solving the full eigenvalue problem in Equation (3.2). Near $S_\varepsilon = 4.66$, two imaginary eigenvalues correspond to a single value of S_ε . Gradually increasing S_ε , these two eigenvalues eventually collide into one. The corresponding S_ε is the saddle node, and the eigenvalue at this point is the saddle eigenvalue. During this process, τ is adjusted to ensure that the eigenvalue(s) remain purely imaginary. The numerical results coincide with the predicted theoretical values.

4.2 The $\tau \sim \mathcal{O}(\varepsilon^{-3})$ regime

In this section, we investigate the instability of the eigenvalue problem for large τ . We assume that $\tau = \varepsilon^{-\alpha} \tau_0$, where $1 \leq \alpha < 3$. With this assumption, we have $\mu = \varepsilon^{\frac{1-\alpha}{2}} \sqrt{\tau_0 \lambda} = \varepsilon^{\frac{1-\alpha}{2}} \mu_0$, where $\mu_0 \sim \mathcal{O}(1)$. Consequently, (4.8)

simplifies to

$$B(\lambda, S_\varepsilon) = -\frac{\varepsilon^{\frac{3-\alpha}{2}} \mu_0 (1/\bar{Q}(\mu) - 1)}{\sqrt{D}(1/\bar{Q}(\mu) + 1)} = \varepsilon^{\frac{3-\alpha}{2}} \mu_0, \quad (4.16)$$

as $1/\bar{Q}(\mu)$ is exponentially small for $\mu \gg 1$. In this case, the leading order of $B(\lambda_I, S_\varepsilon)$ is zero. Therefore, according to the Figure 7, there is no solution to this problem.

Therefore, we consider the scaling of $\tau \sim \mathcal{O}(\varepsilon^{-3})$. Assume that $\tau = \varepsilon^{-3} \tau_0$, so $\mu = \varepsilon^{-1} \sqrt{\tau_0 \lambda} = \varepsilon^{-1} \mu_0$. When $\mu_0 \ll 1$, the leading order of the eigenvalue problem in the inner region is the same as in (4.2). This is the reduced $\tau \sim \mathcal{O}(\varepsilon^{-3})$ regime. Thus, the far-field behavior of Ψ_ε in (4.3) and the matching conditions in (4.8) hold here. We further simplify the matching condition for $\tau_0 \ll 1$, yielding

$$B(\lambda, S_\varepsilon) = \mu_0 = \sqrt{\tau_0 \lambda}. \quad (4.17)$$

Letting $\lambda = \lambda_I i$, equation (4.17) becomes

$$\Re(B(\lambda_I, S_\varepsilon)) = \Im(B(\lambda_I, S_\varepsilon)) = \frac{\sqrt{2\tau_0 \lambda_I}}{2}. \quad (4.18)$$

To Solve (4.18) for a given S_ε , we first solve for λ_I from the first equation where the real part of B equals its imaginary part. In Figure 7, we observe that when $S_\varepsilon > 4.52$, there is one intercept between the real and imaginary curves, located on the branch where $\lambda_I < 1$. We then obtain the value of τ by solving the second equation in (4.18). When $S_\varepsilon = 4.52$, from Figure 7, $\lambda_I = 0$ is the solution to the first equation of (4.18). Letting $\lambda_I = \sigma \lambda_{I1}$ where $\sigma \ll 1$, we then expand B around $(0, 4.52)$, yielding

$$B(0, 4.52) + \sigma \lambda_{I1} B_\lambda(0, 4.52) = \frac{\sqrt{2\tau_0 \sigma \lambda_{I1}}}{2}. \quad (4.19)$$

By collecting the $\mathcal{O}(\sigma)$ terms, we readily see that $\tau_0 = 0$. There is another intercept at $\lambda_I > 1$ for each value of S_ε , as shown in Figure 7. The corresponding τ , however, is large so that the assumption $\mu_0 \ll 1$ is not satisfied. Therefore, these values of τ do not represent an HB threshold in this context. As a result, no HB for $S_\varepsilon < 4.52$ in this regime.

We now consider the case where $\mu_0 \sim \mathcal{O}(1)$. Under this assumption, $\tau_0 \lambda$ is raised to the leading order in the inner region, and the eigenvalue problem becomes

$$\begin{aligned} \Delta_0 \Phi_\varepsilon - \Phi_\varepsilon + 2U_\varepsilon V_\varepsilon \Phi_\varepsilon + V_\varepsilon^2 \Psi_\varepsilon &= \lambda \Phi_\varepsilon, \\ \Delta_0 \Psi_\varepsilon - (2U_\varepsilon V_\varepsilon \Phi_\varepsilon + V_\varepsilon^2 \Psi_\varepsilon) &= \tau_0 \lambda \Psi_\varepsilon, \\ \Phi'_\varepsilon(0) = \Psi'_\varepsilon(0) &= 0; \quad \Phi_\varepsilon \rightarrow 0, \quad \Psi_\varepsilon \rightarrow 0 \quad \text{as } \rho \rightarrow \infty. \end{aligned} \quad (4.20)$$

We define the operator

$$\mathcal{L}_0 = \begin{pmatrix} \Delta_0 \\ \Delta_0/\tau_0 \end{pmatrix} + \begin{pmatrix} -1 + 2U_\varepsilon V_\varepsilon & V_\varepsilon^2 \\ -2U_\varepsilon V_\varepsilon/\tau_0 & V_\varepsilon^2/\tau_0 \end{pmatrix}, \quad (4.21)$$

thus (4.20) can be written as

$$\mathcal{L}_0 \begin{pmatrix} \Phi_\varepsilon \\ \Psi_\varepsilon \end{pmatrix} = \lambda \begin{pmatrix} \Phi_\varepsilon \\ \Psi_\varepsilon \end{pmatrix}. \quad (4.22)$$

A key feature here is that Ψ_ε approaches zero in the far-field, indicating the spot's instability is determined solely by the spectrum of the operator \mathcal{L}_0 . In Figure 10a, we plot the numerically computed dominant (largest real) eigenvalue of \mathcal{L}_0 for various values of S_ε . It is clearly that a zero-crossing as τ_0 increases for each S_ε . The values of τ_0 at which the eigenvalue becomes purely imaginary are then collected, giving the critical threshold τ_H for each S_ε , as shown in Figure 10b. Thus, for a given S_ε , the system is stable to amplitude oscillations when τ_0 is below the critical threshold τ_H but becomes unstable when τ_0 exceeds τ_H . In Figure 10b, we also plot the critical threshold computed from the reduced $\tau \sim \mathcal{O}(\varepsilon^{-3})$ regime. The results from the reduced regime converge increasingly close to those from the full $\mathcal{O}(\varepsilon^{-3})$ regime as S_ε decreases, where $\mu_0 = \tau_0 \lambda \ll 1$.

We now conclude the Hopf bifurcation analysis in the large eigenvalue problem. For the feed rate A ranging from 1 to 60, two regimes of the Hopf bifurcation threshold exist. The first is $\tau \sim \mathcal{O}(1)$, valid for $1 < A < A_\varepsilon$, where $A_\varepsilon > 13.56$ is a saddle point. The second regime is $\tau \sim \mathcal{O}(\varepsilon^{-3})$, valid for $13.56 < A < 60$. Notably, three thresholds

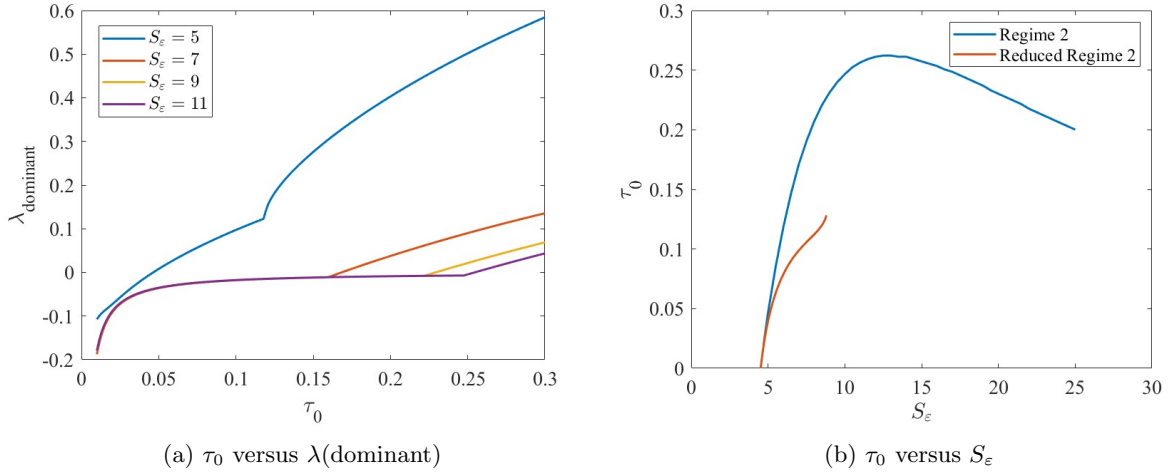


Figure 10: (a) Dominant (largest real) eigenvalues of \mathcal{L}_0 computed numerically, showing a zero-crossing for each value of S_ε . (b) Leading order of the HB threshold versus S_ε for both the reduced $\mathcal{O}(\varepsilon^{-3})$ regime and the full $\mathcal{O}(\varepsilon^{-3})$ regime. The HB threshold in the reduced regime converges to that of the full regime as S_ε decreases.

are observed when $13.56 < A < A_\varepsilon$. A numerical experiment validates this behavior, showing clearly how the instability changes as τ increases within this interval of A . For $A > 60$, the splitting instability occurs and is therefore not considered here. A numerical solution of the full eigenvalue problem in (3.2) is provided in Figure 11 to verify our theoretical result.

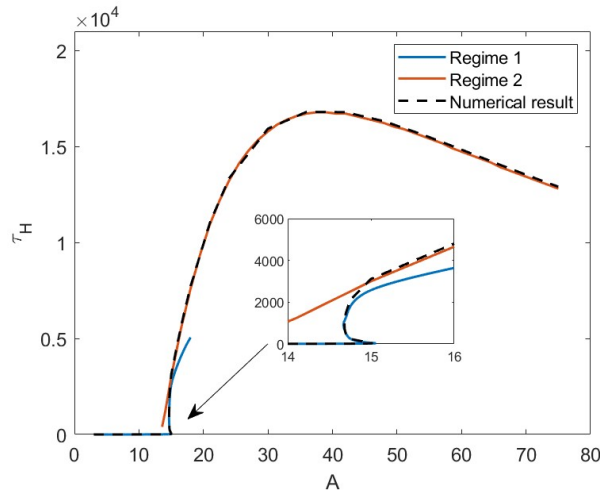


Figure 11: Full theoretical Hopf bifurcation threshold and the full numerical solution by solving (3.2) for $\varepsilon = 0.025$.

5 Numerical validation

In this section, we numerically validate our theoretical result in (3.48) for the small eigenvalue problem and the HB threshold for the large eigenvalue problem by solving the full time-dependent PDE system in (1.2) using the finite element solver FlexPDE 7.

The procedure for verifying the threshold is as follows. We begin by setting τ below any Hopf thresholds, then run the PDE until a sufficiently large time is reached, such that no further changes in the solution are observed. Using this equilibrium solution as an initial condition, we trial various values of τ to test stability. The numerical lower bound τ_{lower} of the Hopf bifurcation threshold is identified when the oscillation amplitude decays and stabilizes at the end, while the numerical upper bound τ_{upper} is identified when the oscillation amplitude grows gradually. In

the asymmetric domain, only the smallest critical τ is tested.

5.1 Hopf bifurcation for small eigenvalue problem

In this section, we examine the theoretical result in (3.48) for the small eigenvalue problem on three domains: a unit sphere, a perturbed sphere, and a sphere with a single ball-shaped defect.

Experiment 1. In this example, we place the problem on a simple, highly symmetric geometry - a unit sphere. In this context, the thresholds are identical for all three directions, resulting in no preferred oscillatory mode. Other parameters are $\varepsilon = 0.03$ and $S_\varepsilon = 15$. The theoretical values computed from Section 3.1 are as follows:

$$\tau_0 = 0.3427, \quad \tau_1 = -0.0688, \quad \tau_2 = 4.7448, \quad \tau = 0.3449. \quad (5.1)$$

We test the stability when $\tau = 0.3448$ and $\tau = 0.3460$ in FlexPDE. The results in Figure 12 show a decaying oscillation for $\tau = 0.3448$ and a growing oscillation for $\tau = 0.3460$.

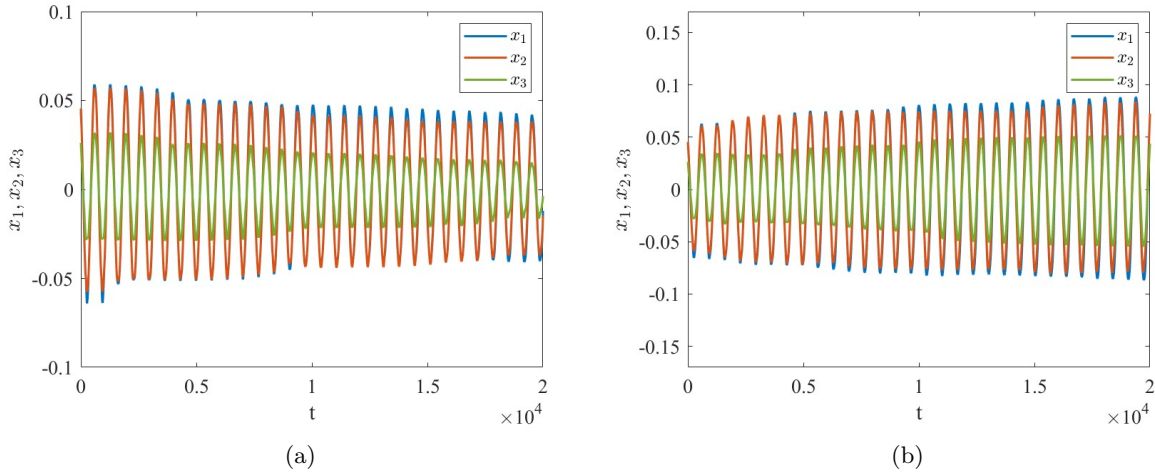


Figure 12: Numerical results from FlexPDE 7 with $\varepsilon = 0.03$ and $S_\varepsilon = 15$. (a) for $\tau = 0.3448$, a decaying oscillation is observed, indicating that τ is below the HB threshold. (b) for $\tau = 0.3460$, a growing oscillation is observed, indicating that τ has exceeded the HB threshold.

Experiment 2. In this example, we chose $\sigma = 0.05$, resulting the perturbation of the domain given by

$$r = (1 + 0.05)f(\theta, \varphi), \quad (5.2)$$

where $f(\theta, \varphi) = \frac{1}{2}(3 \cos^2 \theta - 1)$. This configuration sets the major axis of the geometry along the x_3 -direction

We set $S_\varepsilon = 19$, $\varepsilon = 0.03$ and the initial position of the spot is at the origin. We then solve (3.92) in MATLAB and compare the results with those obtained using FlexPDE under the same parameters and initial position. Due to the geometry's shape, the thresholds τ for the x_1 - and x_2 -directions are identical, while the threshold in the x_3 -direction differs. As expected, two distinct values of τ_{11} are found, corresponding to different oscillatory modes. The positive value indicates oscillation starting in the $x_{1,2}$ -plane, while the negative value corresponds to oscillation along the x_3 -axis.

The theoretical result is

$$\tau_{00} = 0.2512, \quad \tau_{10} = -0.0565, \quad \tau_{11} = -5.1169(3.1779), \quad \tau = 0.2419(0.2543). \quad (5.3)$$

Therefore, as τ increases to reach the $(0, 0, 1)^T$ mode threshold, the spot begins oscillating along the x_3 -axis, which is the preferred mode of oscillatory translational instability.

Experiment 3. In this experiment, we present numerical results for the translational oscillatory instability on a sphere with a single defect. We compare our analytical results obtained using MATLAB with the numerical solution provided by FlexPDE for the same parameters. Here, we set $\varepsilon = 0.03$ and $A = 69$. The defect is positioned at $(-0.5, 0, 0)$, and we set $C = 1$, making the radius of the hole equal to ε (see Figure 14a).

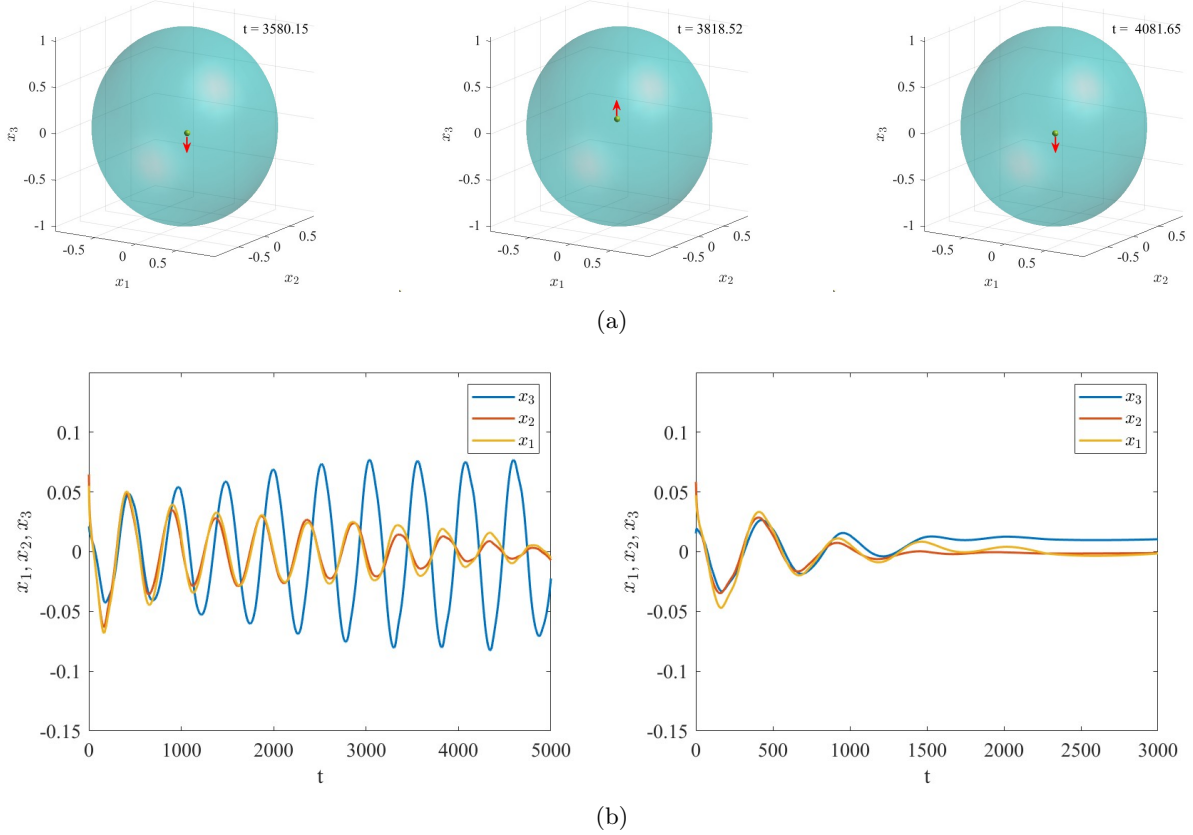


Figure 13: In the top half, we figure out the direction of spot motion with arrows at the particular time. In the bottom half, we plot all three coordinates as functions of time, respectively. Parameters: $S_\varepsilon = 19$, $\varepsilon = 0.03$, $\sigma = 0.05$. Left: $\tau = 0.2540$, $\tau_{11} = 3$. Right: $\tau = 0.2420$, $\tau_{11} = -5$. For increasing time, the x_3 -direction mode (major axis of the domain) emerges as dominant.

By solving the equilibrium problem, we find that the equilibrium position of the spot is $(0.2956, 0, 0)$, with a spot source strength of $S_{\varepsilon_1} = 15.7073$ and a hole source strength of $S_{\varepsilon_0} = 7.2927$. These values match those obtained from FlexPDE.

The leading order threshold τ_0 is determined by the source strength of the spot, S_{ε_1} . Consequently, τ_0 is the same for all three directions, while the preferred direction of translational instability is determined by the first correction of τ . Due to the initial placement of the spot on the x_1 -axis, we expect two distinct thresholds: one corresponding to the x_1 direction and the other to the $x_{2,3}$ directions. The matrix $\mathcal{Q}_{\mu 1}$ is computed by applying central difference on the resulting regular part in (B.5). As a result, $\tau_0 = 0.3230$, while one value of τ_1 is 1.0051 , corresponding to the x_1 direction, and the other is -0.3894 , corresponding to the $x_{2,3}$ directions. In this case, the smaller critical value of τ serves as the HB threshold, beyond which the translational oscillatory instability is triggered. The preferred oscillatory mode at onset is the one along the tangent plane and perpendicular to the x_1 axis. Figure 14b shows the numerical results in FlexPDE for $\tau_1 = 1$. As we expected, the oscillation on x_3 -direction is decaying while that on x_2 -, x_3 -direction are growing, indicating the oscillation mode along $x_{2,3}$ plane is selected as a dominant mode.

5.2 Hopf bifurcation for large eigenvalue problem

In this section, we test the oscillatory instability of the spot's amplitude for the critical τ obtained in Section 4. In the first two experiments, we use FlexPDE to find the lower bound and upper bound for the threshold in each regime. In the last experiment, as we demonstrate in Section 4, there is an overlap between two regimes. We select an intermediate value of A and test the system's stability when τ lies between the two critical values. The aim of this experiment is to understand the behavior of the dominant eigenvalue and the changes in stability as τ increases.

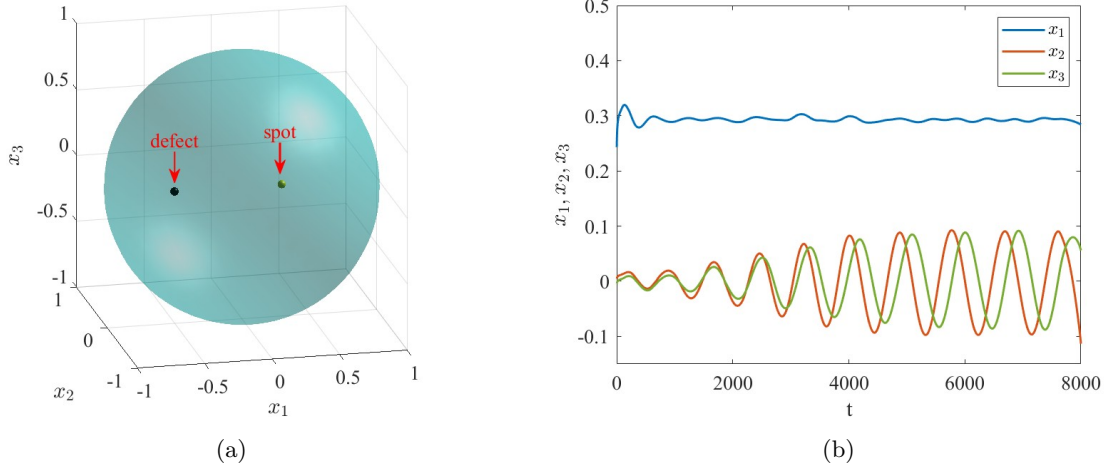


Figure 14: Numerical results for a single-spot pattern with one defect are presented. Parameters are set as $\varepsilon = 0.03$, $A = 69$, and $C = 1$. Figure (a) shows the initial pattern for this experiment: the defect is placed at $(-0.5, 0, 0)$, and the spot is initialized at $(0.2956, 0, 0)$. In (b), with $\tau = 0.3530$ and $\tau_1 = 1$, the oscillation in the x_3 direction is decaying, while oscillations in the x_2 -, x_3 -directions are growing, indicating that the oscillation mode along $x_{2,3}$ -plane is selected as the dominant mode.

Experiment 4. In this experiment, We numerically validate the threshold for the $\tau \sim \mathcal{O}(1)$ regime (regime 1) and the $\tau \sim \mathcal{O}(\varepsilon^{-3})$ regime (regime 2), respectively. Here, we define τ_{upper} and τ_{lower} as the upper and lower bounds of the true threshold, where a growing oscillation in amplitude indicates τ_{upper} and a decaying oscillation indicates τ_{lower} . The 'exact' HB threshold lies between these bounds.

For regime 1, we solve (4.8) from Section 4.1 in a unit ball with $A = 3$ and $\varepsilon = 0.03$, yielding a theoretical value of $\tau_H = 1.4814$. The numerical threshold, as shown in Figure 15a, is between 1.4 and 1.5 which coincide with our theoretical result. We then plot the numerical thresholds for various values of A and compare them to our predicted results in Figure 15b. The theoretical thresholds align closely with the numerical results.

For regime 2, we test the system's instability by setting τ near the theoretical threshold calculated in Section 4.2 for $A = 10$. The theoretical threshold is $\tau_0 = 0.2472$, where $\tau_0 = \varepsilon^3 \tau$ with $\varepsilon = 0.02$. As shown in Figure (15c), the plot shows that the exact value of τ_0 lies between 0.247 to 0.255.

Experiment 5 This experiment aims to investigate amplitude instability in the overlapping region of the two regimes. As τ increases and crosses each threshold, the stability status changes, as analyzed in Section 4. We set $\varepsilon = 0.01$, resulting in a saddle-node at $A_\varepsilon = 14.37$. The experiment is conducted at $A = 14.1$, where three distinct thresholds can be found. Our predicted thresholds are $\tau_H = 13.9956$, $\tau_H = 180.04$, and $\tau_H = 0.0181/\varepsilon^3$ as shown in Figure 16a. We then select four different values of τ : $\tau = 13$, 100 , $0.001/\varepsilon^3$, and $0.02/\varepsilon^3$. These values of τ are examined later in FlexPDE to confirm the stability of the system. In Figure 16b, the left two plots show that the system is stable when $\tau = 13$ and $\tau = 0.001/\varepsilon^3$, while the right two plots indicate that it is unstable when $\tau = 100$ and $\tau = 0.02/\varepsilon^3$. The behavior of the spot's height matches our predictions.

6 Discussion

We have developed a 3×3 complex matrix eigenvalue problem through formal asymptotic analysis, yielding the Hopf bifurcation threshold, oscillatory frequency, and direction of oscillation at the onset of a one-spot pattern equilibrium solution in the Schnakenberg reaction-diffusion system. This result is applicable to both general and defected bounded three-dimensional domains. Additionally, we provide a detailed analysis of parameter values associated with the onset of temporal oscillations in spot amplitudes for the one-spot pattern in this system.

In the small eigenvalue problem, we derived a complex matrix eigenvalue problem. By solving this, we obtained the leading order of the oscillation frequency λ and the bifurcation threshold τ_H at least up to the $\mathcal{O}(\varepsilon)$ correction term.

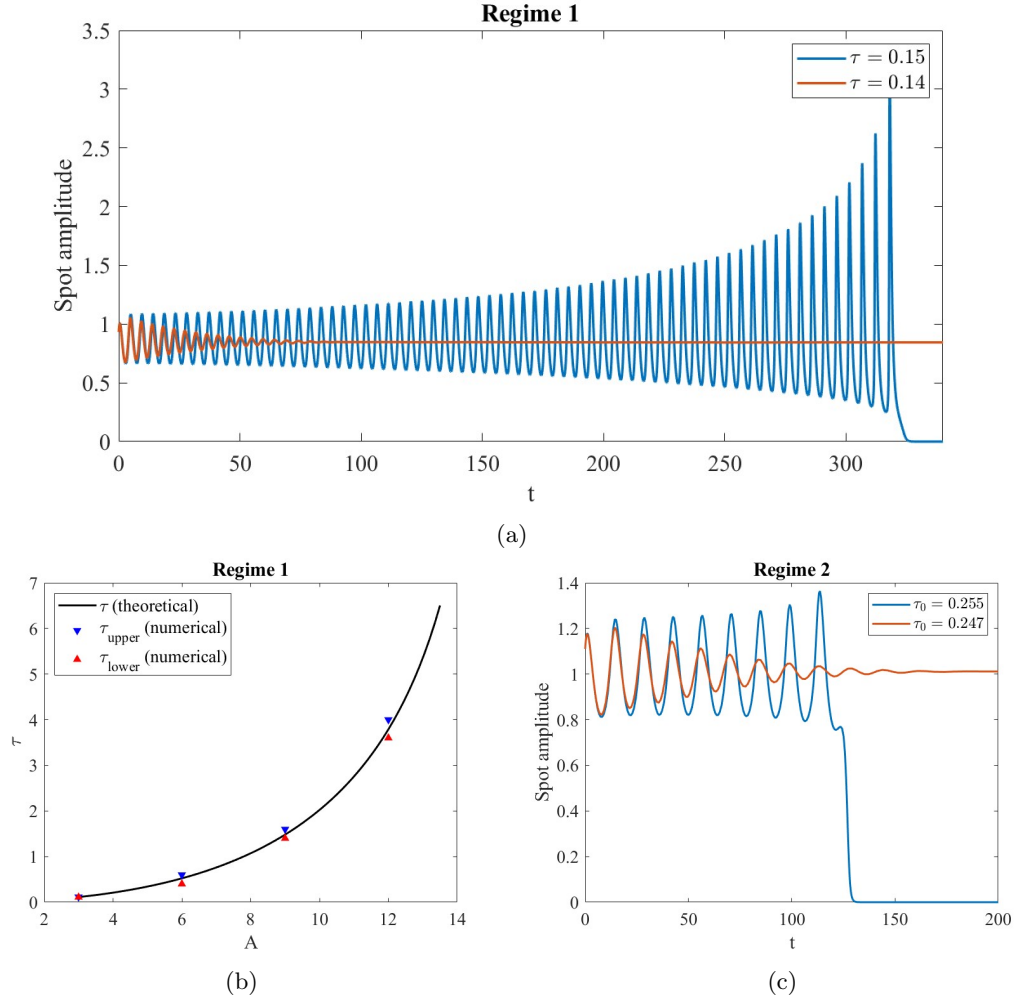


Figure 15: (a) A plot of the spot height from numerically solving (1.2) using FlexPDE7 in a unit ball, with $A = 3$ and $\varepsilon = 0.03$, for the indicated values of τ in regime 1. The exact threshold lies between 1.4 and 1.5. The theoretical threshold 1.4814 aligns closely with the numerical result. (b) A comparison of theoretical and numerical results for various values of A in regime 1, with $\varepsilon = 0.03$. We determine τ_{upper} (τ_{lower}) is the upper(lower) bound of the true threshold when a growing(decaying) oscillation on the amplitude is observed in FlexPDE. (c) A plot validating the leading order of the HB threshold in regime 2. The theoretical value of τ_0 is 0.2472, while numerical predictions suggest it lies between 0.247 and 0.255. Other parameters are set to $A = 10$ and $\varepsilon = 0.02$

We then extended these results to a perturbed sphere with radius in polar coordinates given by $r = 1 + \sigma f(\theta, \varphi)$, where $\theta \in [0, \pi)$, $\varphi \in [0, 2\pi)$, and $\varepsilon \ll \sigma \ll 1$. Here, $f(\theta, \varphi)$ is a Spherical Harmonic function of the form $P_n^m(\cos \theta) \cos m\varphi$. We observed that for $n = 1$, the perturbation on the geometry results in a translation along with an $\mathcal{O}(\sigma^2)$ dilation, which does not affect preferred oscillation direction. For $n \geq 3$, the perturbation does not affect the computation of thresholds. However, for $n = 2$, the geometry is stretched along a specific direction, resulting in an ellipsoid. In this configuration, the spot tends to oscillate along the major axis at onset.

We also examined the problem on a defected sphere. Here, the threshold is closely related to the defect size: a larger defect size increases the threshold, making translational oscillatory instability more difficult to trigger. Moreover, the presence of the defect breaks the high symmetry of the sphere when the defect is not centered. Consequently, the critical value of τ is no longer identical in all three directions. In this case, the smallest critical τ value is defining as the HB threshold.

In the large eigenvalue problem, we analyzed the Hopf bifurcation threshold τ_H in relation to the feed rate A . Two regimes were found in this setup: the $\tau \sim \mathcal{O}(1)$ regime (regime 1) and the $\tau \sim \mathcal{O}(\varepsilon^{-3})$ regime (regime 2). For regime 1, we applied a hybrid asymptotic-numerical method to determine the HB threshold. For regime 2, the threshold

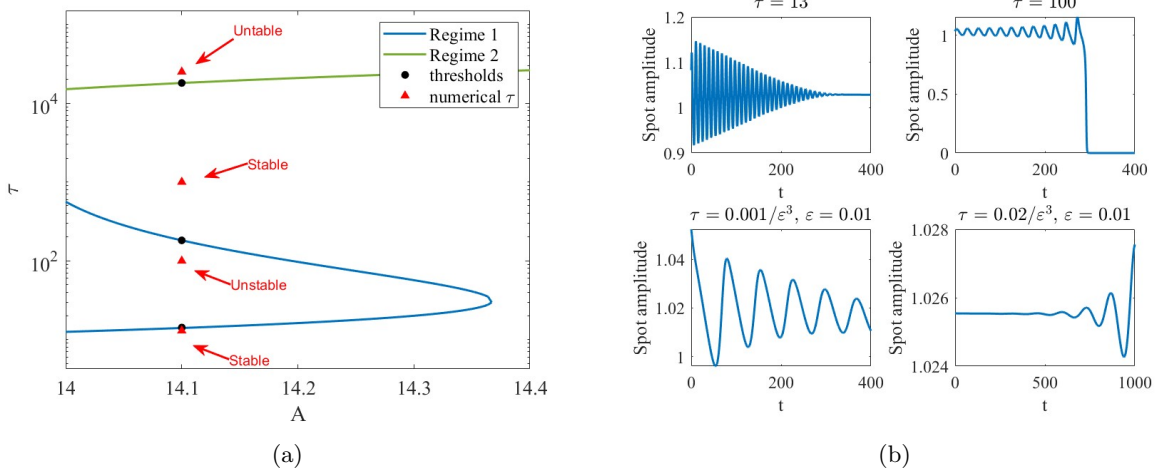


Figure 16: We examine the stability in the overlapping region for $\varepsilon = 0.01$. (a) We set $A = 14.1$, and the three predicted thresholds are $\tau_H = 13.9956$, $\tau_H = 184.04$, and $\tau_H = 0.0181/\varepsilon^2$. We then select four different values of τ : 13, 100, $0.001/\varepsilon^3$, and $0.02/\varepsilon^3$, and predict the stability as indicated. (b) The results of these four τ values in FlexPDE are shown. The left two plots indicate that the system is stable when $\tau = 13$ and $\tau = 0.001/\varepsilon^3$, while the right two plots show that it is unstable when $\tau = 100$ and $\tau = 0.02/\varepsilon^3$. The behavior of the spot's height matches our predictions.

was determined based on the spectrum of the leading order eigenvalue problem in the inner region.

An overlap between these two regimes was observed for a range of A values. Within this interval, as τ increases, the system undergoes a stable-unstable-stable-unstable transition with respect to amplitude oscillatory instability. An interesting finding is an anomalous scaling between the $\mathcal{O}(1)$ regime and the $\mathcal{O}(\varepsilon^{-3})$ regime. In the zoom-in box of Figure 11, a gap between these two regimes is observed, and the scaling of the threshold transitions continuously from $\mathcal{O}(1)$ to $\mathcal{O}(\varepsilon^{-3})$ as A increases. Anomalous scaling for the threshold of temporal spot-height oscillatory instability in the 2D problem has been discussed in [19], and this could serve as a potential direction for future work.

Our analysis was developed for a single-spot pattern in the Schnakenberg model. However, a similar approach could be applied to other activator-inhibitor reaction-diffusion models, such as the Gray-Scott and Brusselator models. Additionally, extending this analysis to multi-spot patterns presents a potential direction for future research.

It would also be interesting to explore other types of heterogeneity in similar problems. The effect of a spatially uniform feed rate on spot height in a 2D problem has been analyzed in [24]. Extending this discussion to the effects on translational and amplitude oscillatory instabilities in a 3D domain would be valuable. Additionally, in our problem, the chemicals' leakage from a defect is modeled by Dirichlet boundary conditions. However, Neumann boundary conditions could be applied if no chemical leakage occurs. In this context, a different type of Green's function, as discussed in [14], would be suitable for modeling this situation during the process of construction the solutions.

Lastly, the relationship between the equilibrium configurations of N -spot patterns in the Schnakenberg model and optimal target configurations in the narrow escape optimization problem has been well investigated in a unit sphere (3D) and a unit disk (2D). (see [1, ?, 24, 21]). It would be worthwhile to explore whether this correspondence persists in more general three-dimensional domains.

Acknowledgement

S. Deng and J.C. Tzou were supported by ARC Discovery Project DP220101808.

A Equilibrium solution of a single spot pattern on a defected domain

The idea here follows [24]. We construct the equilibrium solution for a one-spot pattern problem with one defect on a 3D domain. We assume that $|\mathbf{x}_i - \mathbf{x}_j| = \mathcal{O}(1)$ for $i \neq j$, and $\text{dist}(\mathbf{x}_i, \partial\Omega) = \mathcal{O}(1)$ and $\text{dist}(\mathbf{x}_i, \partial\Omega_\varepsilon) = \mathcal{O}(1)$, where $i = 1$ is the position of the spot and $i = 0$ is the position of the defect.

We then introduce the inner variables

$$\mathbf{y}_j = \frac{\mathbf{x} - \mathbf{x}_j}{\varepsilon} = \rho_j \mathbf{e}_j, \quad \mathbf{e}_j = \begin{pmatrix} \sin \theta_j \cos \varphi_j \\ \sin \theta_j \sin \varphi_j \\ \cos \theta_j \end{pmatrix}, \quad (\text{A.1})$$

$$v_e \sim \sqrt{D}(V_\varepsilon(\rho_j) + \varepsilon^3 V_3(\mathbf{y}_j) + \dots), \quad u_e \sim \frac{1}{\sqrt{D}}(U_\varepsilon(\rho_j) + \varepsilon^3 U_3(\mathbf{y}_j) + \dots),$$

where $j = 0$ representing the defect and $j = 1$ is the spot. $U_{\varepsilon j}, V_{\varepsilon j}$ are weakly depending on ε , and they satisfy the radially symmetric core problem

$$\begin{aligned} \Delta_{\rho_j} V_{\varepsilon j} - V_{\varepsilon j} + U_{\varepsilon j} V_{\varepsilon j}^2 &= 0, & V'_{\varepsilon j}(0) &= 0, \\ \Delta_{\rho_j} U_{\varepsilon j} - U_{\varepsilon j} V_{\varepsilon j}^2 &= 0, & U'_{\varepsilon j}(0) &= 0 \end{aligned} \quad (\text{A.2})$$

with far-field behavior

$$V_{\varepsilon j} \rightarrow 0, \quad U_{\varepsilon j} \sim \chi(S_{\varepsilon j}) - S_{\varepsilon j}/\rho_j + \dots, \quad \text{as } \rho \rightarrow \infty, \quad (\text{A.3})$$

Applying the divergence theorem on the second equation of (A.2), we have

$$S_{\varepsilon j} = \int_0^\infty U_{\varepsilon j} V_{\varepsilon j}^2 \rho_j^2 d\rho_j. \quad (\text{A.4})$$

Now we use strong localized perturbation theory to replace the effect of the defect with Dirac singularity. Let

$$\mathbf{y}_0 = \varepsilon^{-1}(\mathbf{x} - \mathbf{x}_0) \quad \text{and} \quad U \sim \frac{U_{\varepsilon 0}}{\sqrt{D}}, \quad (\text{A.5})$$

where $U_{\varepsilon 0}$ is $\mathcal{O}(1 + \varepsilon)$, the leading order hence satisfies

$$\Delta_{\mathbf{y}_0} U_{\varepsilon 0} = 0, \quad |\mathbf{y}_0| \geq C; \quad U_{\varepsilon 0} = 0 \quad \text{on} \quad |\mathbf{y}_0| = C. \quad (\text{A.6})$$

We emphasize that $V_{\varepsilon 0}$ near the defect is zero because $V_{\varepsilon 0} = 0$ when $|\mathbf{y}_0| = C$ and the far-field of $V_{\varepsilon 0}$ is also zero.

The solution to (A.6) is $U_{\varepsilon 0} = S_{\varepsilon 0} \left(\frac{1}{C} - \frac{1}{|\mathbf{y}_0|} \right)$, where $S_{\varepsilon 0}$ to be determined. It gives the local behavior of the outer u , which is

$$u \sim \frac{S_{\varepsilon 0}}{\sqrt{D}} \left(\frac{1}{C} - \frac{\varepsilon}{|\mathbf{x} - \mathbf{x}_0|} \right), \quad \text{as } \mathbf{x} \rightarrow \mathbf{x}_0. \quad (\text{A.7})$$

Therefore, we have the identity

$$\int_{\partial\Omega_\varepsilon} -D \partial_n u|_{\partial\Omega_\varepsilon} ds \sim 4\pi S_{\varepsilon 0} \sqrt{D}, \quad (\text{A.8})$$

where ∂_n is the outward normal derivative to $\bar{\Omega}$. That implies the constant $S_{\varepsilon 0}$ is proportional to the diffusive flux of inhibitor through the defect.

By imposing the Dirac singularity $\frac{4\pi S_{\varepsilon 0}}{\sqrt{D}} \delta(\mathbf{x} - \mathbf{x}_0)$ on the outer problem and expanding $u \sim u_0 + \varepsilon u_1$, we obtain, in $\mathcal{O}(\varepsilon)$,

$$\begin{aligned} D\Delta u_1 + A &= 4\pi \left[S_{\varepsilon 1} \delta(\mathbf{x} - \mathbf{x}_1) + S_{\varepsilon 0} \delta(\mathbf{x} - \mathbf{x}_0) \right] \quad \text{in } \Omega; \\ \partial_n u_1 &= 0 \quad \text{on } \partial\Omega. \end{aligned} \quad (\text{A.9})$$

The solution to (A.9) is represented in terms of the Neumann Green's function as

$$u_1 = -\frac{4\pi}{\sqrt{D}}(S_{\varepsilon 1}G(\mathbf{x}; \mathbf{x}_1) + S_{\varepsilon 0}G(\mathbf{x}; \mathbf{x}_0)) + \bar{u}_1, \quad (\text{A.10})$$

where $G(\mathbf{x}; \mathbf{x}_j)$ satisfies (2.8). Therefore, u can be expressed as

$$u = u_0 + \varepsilon\left(\bar{u}_1 - \frac{4\pi}{\sqrt{D}}(S_{\varepsilon 1}G(\mathbf{x}; \mathbf{x}_1) + S_{\varepsilon 0}G(\mathbf{x}; \mathbf{x}_0))\right). \quad (\text{A.11})$$

By applying the divergence theorem to (A.9) we get

$$S_{\varepsilon 1} + S_{\varepsilon 0} = \frac{A|\Omega|}{4\pi\sqrt{D}}. \quad (\text{A.12})$$

We next complete the matching by analysing the local behavior at the spot and the defect, respectively. Further to determine the constant, we find the expanding form of the local behavior of the outer solution. When $\mathbf{x} \rightarrow \mathbf{x}_0$, we substitute the local behavior of the Green's function given in (2.8) into (A.11) and match with (A.7), yielding

$$u_0 + \varepsilon\bar{u}_1 - \frac{4\pi\varepsilon S_{\varepsilon 0}}{\sqrt{D}}R(\mathbf{x}_0; \mathbf{x}_0) - \frac{4\pi\varepsilon S_{\varepsilon 1}}{\sqrt{D}}G(\mathbf{x}_0; \mathbf{x}_1) = \frac{S_{\varepsilon 0}}{C\sqrt{D}}. \quad (\text{A.13})$$

Recall that the far-field of $U_{\varepsilon 1}$ in the core problem is given by $U_{\varepsilon 1} \sim \chi(S_{\varepsilon 1}) - \frac{\varepsilon S_{\varepsilon 1}}{|\mathbf{x} - \mathbf{x}_1|}$. Similarly, when $\mathbf{x} \rightarrow \mathbf{x}_1$, we have

$$u_0 + \varepsilon\bar{u}_1 - \frac{4\pi\varepsilon S_{\varepsilon 1}}{\sqrt{D}}R(\mathbf{x}_1; \mathbf{x}_1) - \frac{4\pi\varepsilon S_{\varepsilon 0}}{\sqrt{D}}G(\mathbf{x}_1; \mathbf{x}_0) = \chi(S_{\varepsilon 1}). \quad (\text{A.14})$$

Since we treat the defect as a pinned spot in our analysis, we then use the equilibrium condition given in [17], which is

$$\frac{d\mathbf{x}_1}{dt} = -\frac{12\pi\varepsilon^3}{k_1}(S_{\varepsilon 1}\nabla_{\mathbf{x}}R(\mathbf{x}_1; \mathbf{x}_1) + S_{\varepsilon 0}\nabla_{\mathbf{x}}G(\mathbf{x}_1; \mathbf{x}_0)). \quad (\text{A.15})$$

By solving (A.12), (A.13), (A.14) and (A.15) simultaneously, we obtain the source strength of the spot $S_{\varepsilon 1}$, the source strength of the hole $S_{\varepsilon 0}$, the equilibrium position of the spot, and all other constants.

B The regular part of the Helmholtz Green's function

In this section, we derive $\mathcal{Q}_{\mu 1}$ for the computation in Section 3.3. The approach begins with constructing a general form of the Helmholtz Green's function G_{μ} solution using a Fourier series which satisfies (1.3). To isolate the regular part, we use the expression $G_{\mu} - G_{\mu f} + R_{\mu f}$, where $G_{\mu f}$ represents the corresponding free space Helmholtz Green's function, and $R_{\mu f}$ is its regular part

We begin by expressing the Helmholtz Green's function. Using separation of variables, we solve for $G_{\mu}(\mathbf{x}; \mathbf{x}_0)$ in (1.3) and represent it in polar series form, with $\mathbf{x} = \rho\mathbf{e}$ and $\mathbf{x}_0 = \rho_0\mathbf{e}_0$, where \mathbf{e}_j is defined in (A.1), yielding

$$G_{\mu}(\rho; \phi; \theta; \rho_0; \phi_0; \theta_0) = \sum_{n=0}^{\infty} A_{\mu n}(\rho, \rho_0) \sum_{m=0}^n Y_n^m(\phi, \theta, \phi_0, \theta_0), \quad (\text{B.1})$$

where

$$A_{\mu n}(\rho, \rho_0) = (2n+1)\rho^{-\frac{1}{2}}\rho_0^{-\frac{1}{2}} \begin{cases} [Q_q(\mu)I_q(\mu\rho_0) + K_q(\mu\rho_0)]I_q(\mu\rho), & 0 \leq \rho < \rho_0 \\ [Q_q(\mu)I_q(\mu\rho) + K_q(\mu\rho)]I_q(\mu\rho_0), & \rho_0 \leq \rho \leq 1 \end{cases}, \quad (\text{B.2})$$

$$Y_n^m(\phi, \theta, \phi_0, \theta_0) = cP_n^m(\cos\theta)P_n^m(\cos\theta_0)\cos[m(\phi - \phi_0)].$$

Here, $I_q(z)$ and $K_q(z)$ are the first and second kind of modified Bessel function, respectively, and $q = n + \frac{1}{2}$, $Q_q(\mu) = -\frac{2\mu K_q'(\mu) - K_q(\mu)}{2\mu I_q'(\mu) - I_q(\mu)}$. The constant coefficient c is given by $c = -\frac{1}{4\pi}$ when $m = 0$, and $c = -\frac{1}{2\pi} \frac{(n-m)!}{(n+m)!}$ when $m \geq 1$.

In a free domain, the exact solution of the Helmholtz Green's PDE in 3D is given by $G_{\mu f} = -\frac{e^{-\mu|\mathbf{x}-\mathbf{x}_0|}}{4\pi|\mathbf{x}-\mathbf{x}_0|}$. To make $R_{\mu}(\mathbf{x}; \mathbf{x}_0)$ consistent, we write $G_{\mu f}$ in a polar series form. Hence we have

$$G_{\mu f}(\rho; \phi; \theta; \rho_0; \phi_0; \theta_0) = \sum_{n=0}^{\infty} A_{fn}(\rho, \rho_0) \sum_{m=0}^n Y_n^m(\phi, \theta, \phi_0, \theta_0),$$

$$A_{fn} = (2n+1)\rho^{-\frac{1}{2}}\rho_0^{-\frac{1}{2}} \begin{cases} K_q(\mu\rho_0)I_q(\mu\rho), & 0 \leq \rho < \rho_0 \\ K_q(\mu\rho)I_q(\mu\rho_0), & \rho_0 \leq \rho \leq 1. \end{cases} \quad (\text{B.3})$$

By applying a Taylor expansion to the exact form of $G_{\mu f}$, the regular part of $G_{\mu f}$ is readily obtained as

$$R_{\mu f} = \frac{\mu}{4\pi} + \frac{\mu^3}{24\pi}|\mathbf{x} - \mathbf{x}_0|^2. \quad (\text{B.4})$$

Therefore, the regular part of Helmholtz Green's function is

$$R_{\mu}(\rho; \phi; \theta; \rho_0; \phi_0; \theta_0) = \frac{\mu}{4\pi} + \frac{\mu^3}{24\pi}|\mathbf{x} - \mathbf{x}_0|^2 + \sum_{n=0}^{\infty} A_n(\rho, \rho_0) \sum_{m=0}^n Y_n^m(\phi, \theta, \phi_0, \theta_0), \quad (\text{B.5})$$

where

$$A_n(\rho, \rho_0) = (2n+1)Q_q(\mu)I_q(\mu\rho_0)I_q(\mu\rho)\rho^{-\frac{1}{2}}\rho_0^{-\frac{1}{2}}, \quad (\text{B.6})$$

and Y_n^m is defined in (B.2). We emphasize that only one branch remains in R_{μ} due to its inherent symmetry.

References

- [1] Paul C. Bressloff. Asymptotic analysis of target fluxes in the three-dimensional narrow capture problem. *Multiscale Model. Simul.*, 19:612–632, 2020.
- [2] Tamás Bánsági, Vladimir K. Vanag, and Irving R. Epstein. Tomography of reaction-diffusion microemulsions reveals three-dimensional turing patterns. *Science*, 331(6022):1309–1312, 2011.
- [3] W. Chen and M. J. Ward. The stability and dynamics of localized spot patterns in the two-dimensional Gray–Scott model. *SIAM Journal on Applied Dynamical Systems*, 10(2):582–666, 2011.
- [4] WAN CHEN and MICHAEL J. WARD. Oscillatory instabilities and dynamics of multi-spike patterns for the one-dimensional Gray-Scott model. *European Journal of Applied Mathematics*, 20(2):187–214, 2009.
- [5] PW Davies, P Blanchedeau, E Dulos, and P De Kepper. Dividing blobs, chemical flowers, and patterned islands in a reaction- diffusion system. *The Journal of Physical Chemistry A*, 102(43):8236–8244, 1998.
- [6] Arjen Doelman, Wiktor Eckhaus, and Tasso J. Kaper. Slowly modulated two-pulse solutions in the Gray-Scott model i: Asymptotic construction and stability. *SIAM Journal on Applied Mathematics*, 61(3):1080–1102, 2000.
- [7] A. Gierer and H. Meinhardt. A theory of biological pattern formation. *Kybernetik*, 12:30–39, Dec 1972.
- [8] Daniel Gomez, Michael Jeffrey Ward, and Juncheng Wei. An asymptotic analysis of localized three-dimensional spot patterns for the Gierer-Meinhardt model: Existence, linear stability, and slow dynamics. *SIAM J. Appl. Math.*, 81:378–406, 2020.
- [9] Robert A. Van Gorder. Pattern formation from spatially heterogeneous reaction–diffusion systems. *Philosophical Transactions of the Royal Society A*, 379, 2021.
- [10] Yuta Ishii. Stability of multi-peak symmetric stationary solutions for the Schnakenberg model with periodic heterogeneity. *Communications on Pure & Applied Analysis*, 2020.
- [11] T. Kolokolnikov, M. J. Ward, and J. Wei. Slow translational instabilities of spike patterns in the one-dimensional Gray-Scott model. *Interfaces and Free Boundaries, Mathematical Analysis, Computation and Applications*, 8:185–222, 2006.
- [12] T. Kolokolnikov, M. J. Ward, and J. Wei. Spot self-replication and dynamics for the Schnakenburg model in a two-dimensional domain. *Journal of Nonlinear Science*, 19(1):1–56, 2009.

- [13] Theodore Kolokolnikov, Michael J. Ward, and Juncheng Wei. The existence and stability of spike equilibria in the one-dimensional Gray–Scott model: The pulse-splitting regime. *Physica D: Nonlinear Phenomena*, 202(3):258–293, 2005.
- [14] Vladimir Maz’ya and Alexander Movchan. *Uniform Asymptotics of Green’s Kernels for Mixed and Neumann Problems in Domains with Small Holes and Inclusions*, pages 277–316. Springer New York, New York, NY, 2009.
- [15] H. Meinhardt. Models of biological pattern formation. *Academic Press*, 1982.
- [16] J. Schnakenberg. Simple chemical reaction systems with limit cycle behaviour. *Journal of Theoretical Biology*, 81(3):389–400, 1979.
- [17] J. Tzou, S. Xie, T. Kolokolnikov, and M. J. Ward. The stability and slow dynamics of localized spot patterns for the 3-D Schnakenberg reaction-diffusion model. *SIAM Journal on Applied Dynamical Systems*, 16:294–336, 01 2017.
- [18] J. C. TZOU, A. BAYLISS, B. J. MATKOWSKY, and V. A. VOLPERT. Stationary and slowly moving localised pulses in a singularly perturbed Brusselator model. *European Journal of Applied Mathematics*, 22(5):423–453, 2011.
- [19] J. C. Tzou, M. J. Ward, and J. C. Wei. Anomalous scaling of hopf bifurcation thresholds for the stability of localized spot patterns for reaction-diffusion systems in two dimensions. *SIAM Journal on Applied Dynamical Systems*, 17(1):982–1022, 2018.
- [20] J C Tzou and S Xie. Oscillatory translational instabilities of spot patterns in the Schnakenberg system on general 2D domains. *Nonlinearity*, 36(5):2473, Mar 2023.
- [21] Justin C. Tzou and Theodore Kolokolnikov. Mean first passage time for a small rotating trap inside a reflective disk. *Multiscale Model. Simul.*, 13:231–255, 2014.
- [22] Michael Ward and J. WEI. Hopf bifurcation of spike solutions for the shadow Gierer–Meinhardt model. *European Journal of Applied Mathematics*, 14:677 – 711, 12 2003.
- [23] Juncheng Wei and Matthias Winter. Spikes for the Gierer–Meinhardt system in two dimensions: The strong coupling case. *Journal of Differential Equations*, 178(2):478–518, 2002.
- [24] T. Wong and M. J. Ward. Spot patterns in the 2-D Schnakenberg model with localized heterogeneities. *Studies in Applied Mathematics*, 146(4):779–833.
- [25] Shuangquan Xie and Theodore Kolokolnikov. Moving and jumping spot in a two-dimensional reaction–diffusion model. *Nonlinearity*, 30(4):1536, mar 2017.